Neural dynamics, bifurcations and firing rates in a quadratic integrate-and-fire model with a recovery variable. I: deterministic behavior

Eli Shlizerman[1] and Philip Holmes[2]
[1] Department of Applied Mathematics,
University of Washington, Seattle, WA 98195-2420, U.S.A.
[2] Program in Applied and Computational Mathematics,
Department of Mechanical and Aerospace Engineering
and Princeton Neuroscience Institute,
Princeton University, Princeton, NJ 08544-1000, U.S.A.

November 23, 2011

Abstract

We study the dynamics of a quadratic integrate-and-fire model of a single compartment neuron with a slow recovery variable, as input current and parameters describing timescales, recovery variable, and post-spike reset change. Analysis of a codimension two bifurcation reveals that the domain of attraction of a stable hyperpolarized rest state interacts subtly with reset parameters, which reposition the system state after spiking. We obtain explicit approximations of instantaneous firing rates for fixed values of the recovery variable, and use the averaging theorem to obtain asymptotic firing rates as a function of current and reset parameters. Along with the different phase plane geometries, these computations provide explicit tools for the interpretation of different spiking patterns, and to guide parameter selection in modeling different cortical cell types.

Running title: Dynamics of a planar quadratic integrate-and-fire model
Key words: asymptotic firing rates, averaging, codimension two bifurcation, cortical cell responses, instantaneous firing rates, slow-fast dynamics.
AMS subject classifications: 34A38, 34C20, 34C23, 34C37, 37Gxx, 92C20

1 Introduction

A wide variety of differential equations have been proposed to model neurons. These range from biophysically-based descriptions involving nonlinear dynamics of multiple ion channels as pioneered by Hodgkin and Huxley (Hodgkin and Huxley, 1952), to linear integrate-and-fire models, in which only the subthreshold membrane voltage is tracked, and action potentials (spikes) are replaced by a stereotypical delta functions followed by voltage reset below threshold. While the details of channel dynamics and timescales of different ionic species are important in determining spike-generation mechanisms and post-spiking refractory periods, reduced models are widely used in simulating large networks. Less radical simplifications of ion-channel models have also been derived

(e.g. (FitzHugh, 1961; Nagumo et al., 1962; Rinzel, 1985)), in which the fastest channels are assumed to be equilibrated, and only membrane voltage and a slow recovery variable are retained, permitting phase plane analyses (Guckenheimer and Holmes, 1983). For background, see texts such as (Keener and Sneyd, 1998; Wilson, 1999; Ermentrout and Terman, 2010).

In this paper we analyze a quadratic integrate-and-fire model, a hybrid dynamical system with a recovery variable, due to Izhikevich, that combines rich subthreshold dynamics with variable reset locations in the phase plane (Izhikevich, 2003, 2006). Previous analysis (Touboul, 2008; Touboul and Brette, 2009) revealed a codimension two Takens-Bogdanov bifurcation (Guckenheimer and Holmes, 1983) which organizes branches of saddle-node, Andronov-Hopf, and homoclinic bifurcations. The resulting dynamics includes hyperpolarized rest states that may be stable or unstable, a branch of unstable limit cycles, and a homoclinic loop to a saddle-type threshold state. With suitable parameter choices, this system can reproduce diverse spiking patterns observed in many types of cortical neurons; see, e.g., (Izhikevich, 2006, Ch. 8) and (Izhikevich, 2010).

For sufficiently high constant input currents, no fixed points exist, and with appropriate reset parameters the system exhibits transient behavior that eventually settles to periodic spiking or bursting. In this paper we characterize the transient dynamics by computing *instantaneous* firing rates for a constant input current and fixed recovery variable, based on the first interspike interval after reset at a particular location. We show that firing rates do not rise from zero at a critical current, as for scalar integrate-and-fire models, and finite firing rates persist over a wide current range, resembling those of integrate-and-fire models with additive noise.

Using the instantaneous firing rates and averaging theory for differential equations, we then compute *asymptotic* firing rates that are obtained for fixed parameter values, after the hybrid dynamics settles to a stable periodic orbit. These yield families of firing rate curves as a function of input current, depending on reset parameters. The instantaneous and asymptotic firing rates provide accurate and explicit guidelines to determine feasible behaviors, and thus predict which types of neural responses the model can reproduce. Phase plane geometry also guides parameter selection: for example, when a stable fixed point is present but post-spike resets fall outside its domain of attraction, decaying subthreshold oscillations and persistent spiking coexist in a bistable system. Moreover, input current steps and impulses can evoke varied combinations of transients and periodic spiking that resemble numerous observed patterns.

We briefly describe scalar integrate-and-fire models in §2 before introducing the quadratic model with recovery variable and reviewing its dynamics and bifurcations in §3.1. We use these and the system's fast-slow dynamics to derive explicit approximations of instantaneous firing rates in §3.2, and of asymptotic firing rates as fixed points of an averaged differential equation in §3.3. In §4 we draw on these analyses to explain a variety of responses to constant current and impulsive inputs, and to select appropriate parameter sets to illustrate them. A discussion follows in §5. Details of bifurcation calculations and proofs and computations involved in the firing rate and fixed point analyses are given in the Appendix.

2 The quadratic integrate-and-fire model

The quadratic integrate-and-fire model with a recovery variable (RQIF) generalizes the quadratic integrate-and-fire model (QIF), which was proposed as an alternative to the simpler leaky integrate-and-fire model (LIF). We start by briefly reviewing the LIF.

2.1 The leaky integrate-and-fire model

The leaky integrate-and-fire model may be written as

$$\begin{aligned} &C\dot{V} = -g_L(V - V_L) + I; \quad V(t) \in [V_{reset}, V_{thresh}], \\ &\text{when } \; V(t) = V_{thresh}, \text{ insert } \delta(t) \text{ and set } V = V_{reset}, \end{aligned} \tag{1}$$

where V denotes the transmembrane potential, C its capacitance, g_L a leak conductance, and I the input current (Stein, 1965; Knight, 1972). In (1) the rapid action potential (AP or spike) is replaced by a delta function that occurs when the voltage V reaches threshold V_{thresh}, immediately after which V is re-initialized at V_{reset}.

Letting V_{ss} denote the steady state that the system would approach in the absence of V_{thresh}, the differential equation of (1) can be rewritten as:

$$\frac{C}{g_L}\dot{V} = -V + V_{ss}, \text{ where } V_{ss} = V_L + \frac{I}{g_L}, \tag{2}$$

and for constant input current I such that $V_{ss} > V_{reset}$, its interspike interval (ISI) can be calculated as

$$T = \frac{C}{g_L}\int_{V_{reset}}^{V_{thresh}} \frac{dV}{V_{ss} - V} = \frac{C}{g_L} \ln\left[\frac{V_{ss} - V_{reset}}{V_{ss} - V_{thresh}}\right]. \tag{3}$$

The firing rate $\phi(I)$ is simply the inverse of ISI, specifically:

$$\phi(I) = \begin{cases} 0 & \text{if } V_{ss} \le V_{thresh} \\ \frac{1}{T} & \text{if } V_{ss} > V_{thresh} \end{cases}; \tag{4}$$

an example is shown in Fig. 1(a). A refractory period τ_{ref} is sometimes included following reset before allowing the solution to continue, thus determining a maximum firing rate.

The LIF model is simple and useful, but it does not encode the actual potential V reached during the AP, and its subthreshold dynamics cause $V(t)$ to decelerate as it approaches V_L. This makes LIF firing rates rise more rapidly from zero for small $V_{ss} - V_{thresh}$ than is typically observed, due to the logarithmic singularity in (3) (Fig. 1(a)) (Connor et al., 1977; Rinzel and Ermentrout, 1989). The QIF model repairs these deficits by using quadratic voltage dependence, which accelerates $V(t)$ to infinity in finite time, allowing one to define a peak voltage prior to reset and producing a slower rise in $\phi(I)$. In reality, input currents are nonconstant and noisy, which permits the LIF model to fire for subthreshold mean currents and effectively smooths $\phi(I)$ (Wan and Tuckwell, 1982; Amit and Tsodyks, 1991), but the low noise LIF limit still exhibits a rapid rise.

2.2 The quadratic integrate-and-fire model: definition and firing rates

The quadratic integrate-and-fire (QIF) or "theta-model" was introduced by Ermentrout and Kopell (Ermentrout and Kopell, 1986). In nondimensional form (indicated by lowercase v) it can be defined as follows:

$$\begin{aligned} &\dot{v} = v^2 + I; \\ &\text{if} \quad v = v_{peak}, \text{ set } v = v_{reset}. \end{aligned} \tag{5}$$

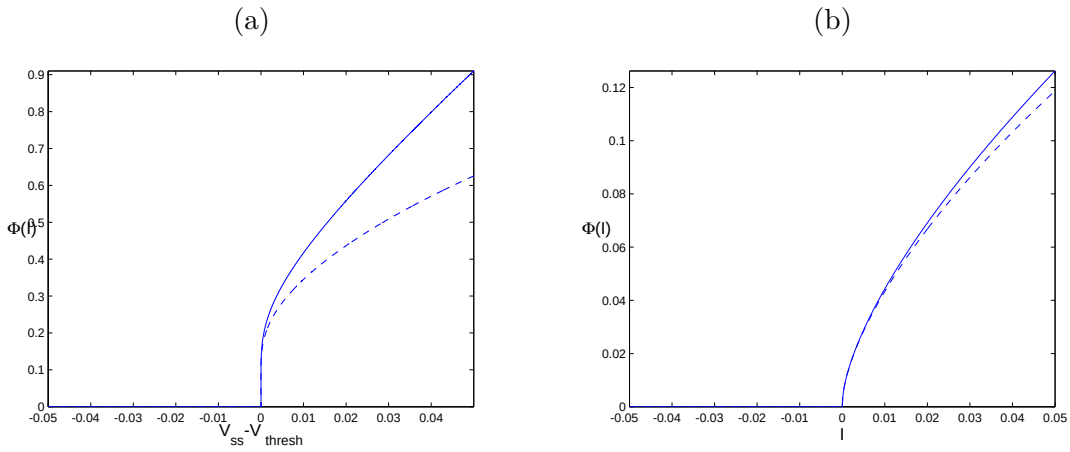

Figure 1: Firing rate curves for the LIF and QIF models. (a): Firing rate curve for the LIF neuron (Eqs. (3-4), solid) with parameters $V_{reset} = 0, V_L = -0.1, V_{thresh} = 0.1$ and $C/g_L = 1$, and firing rate with refractory period $\tau_{ref} = 0.5$ (dashed). (b): Firing rate curve for the QIF neuron (Eq. (7), solid) with $V_{reset} = -0.1$ and $V_{peak} = 1$, and firing rate with refractory period $\tau_{ref} = 0.5$ (dashed).

Voltage is reset when v reaches v_{peak}, thus defining the maximum spike voltage.

The theta model of (Ermentrout and Kopell, 1986) can be obtained from (5) by the transformation $v = \tan(\theta/2)$:

$$\dot{\theta} = 1 - \cos\theta + (1 + \cos\theta)I, \tag{6}$$

where $\theta \in [0, 2\pi)$ denotes a phase variable. The inverse transformation to v is singular at $\theta = \pi$ so that $v \to \infty$. Thus, a spike is emitted each time $\theta(t)$ passes π and no reset rule is needed, since the phase space is periodic. As shown in (Ermentrout and Kopell, 1986), Eq. (6) has a saddle-node bifurcation that occurs on the invariant circle, the normal form of which is Eq. (5). This indicates that Eq. (5) is generic in the sense that it describes the near-threshold dynamics of any other model that possess such a codimension one bifurcation (Guckenheimer and Holmes, 1983).

For $I > 0$ Eq. (5) has no fixed points and exhibits periodic spiking with ISI

$$T = \int_{v_{reset}}^{v_{peak}} \frac{dv}{v^2 + I} = \frac{1}{\sqrt{I}} \operatorname{atan}\left(\frac{v}{\sqrt{I}}\right)\Big|_{v_{reset}}^{v_{peak}} = \frac{1}{\sqrt{I}} \operatorname{atan}\left[\frac{\sqrt{I}(v_{peak} - v_{reset})}{I + v_{peak} v_{reset}}\right] : \tag{7}$$

see Fig. 2 (bottom). An example of the resulting firing rate $\phi(I) = 1/T$ appears in Fig. 1(b): note the slower increase from $I = 0$, compared to the LIF. The parabola-like QIF curve better fits the steady state current-voltage $I_\infty(v)$ characteristics of many types of neurons, as well as that of the Hodgkin-Huxley equations (Hodgkin and Huxley, 1952).

When $I < 0$, a pair of fixed points $v_f = \pm\sqrt{|I|}$ appears. The positive one, $v_{thresh} = \sqrt{|I|}$, is unstable and denotes a threshold value; the negative one, $v_{rest} = -\sqrt{|I|}$, is stable and represents the resting potential: see Fig. 2 (top). For $v_{reset} > v_{thresh}$ the model still exhibits periodic firing with ISI

$$T = \int_{v_{reset}}^{v_{peak}} \frac{dv}{v^2 - |I|} = \frac{1}{2\sqrt{|I|}} \ln\left[\frac{\left(v_{peak} - \sqrt{|I|}\right)\left(v_{reset} + \sqrt{|I|}\right)}{\left(v_{peak} + \sqrt{|I|}\right)\left(v_{reset} - \sqrt{|I|}\right)}\right] : \tag{8}$$

see Fig. 2 (center). For $v_{reset} < v_{thresh}$, voltage is reset in the basin of attraction of the stable fixed point: Fig. 2 (top). No periodic solution exists, but the neuron is excitable: superthreshold perturbations of magnitude exceeding $|v_{thresh} - v_{reset}|$ can cause it to fire and return to the resting state. Similarly, for $v_{reset} > v_{thresh}$ sufficiently large negative perturbations can terminate firing. At $v_{reset} = v_{thresh}$ a "hybrid homoclinic bifurcation" occurs, in which the spiking solution departs from threshold and is reset at threshold.

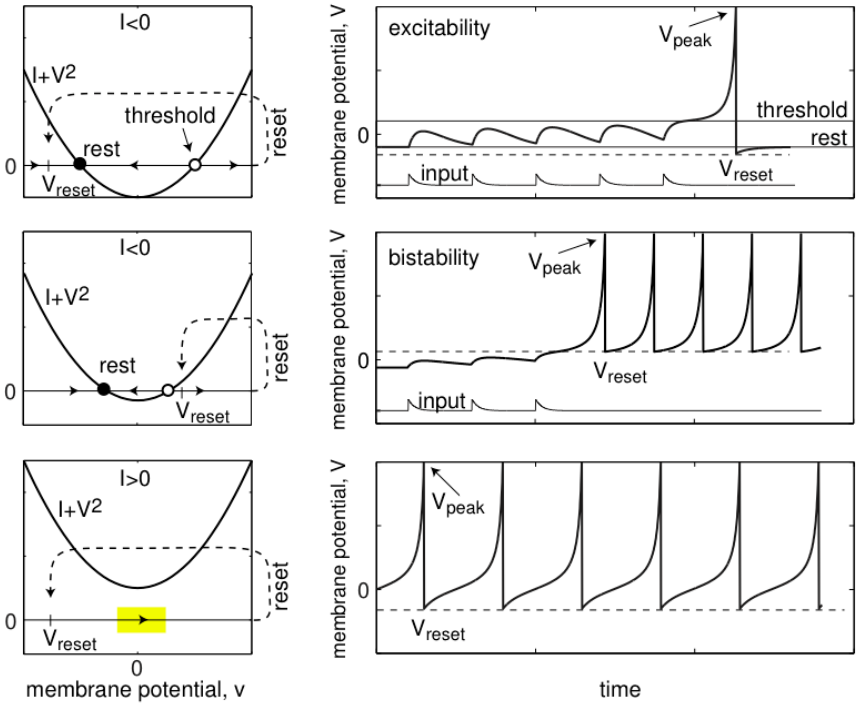

Figure 2: Vector fields, 1-dimensional phase portraits, and voltage traces for the quadratic integrate-and-fire neuron for $I > 0$ and $I < 0$, showing effects of different reset parameters. Reproduced from (Izhikevich, 2006), Fig. 3.35.

3 The quadratic integrate-and-fire model with recovery variable

In (Izhikevich, 2003) Izhikevich extended the QIF model by introducing a recovery variable u in the spirit of FitzHugh's approximation of the Hodgkin-Huxley equations (FitzHugh, 1961). After rescaling, this so-called simple model can be written as

$$\begin{aligned} \dot{v} &= v^2 - u + I, \\ \dot{u} &= a(bv - u); \\ \text{if} \quad & v \geq v_{peak}, \text{ set } v = c, \ u = u + d. \end{aligned} \tag{9}$$

This two-dimensional system has five independent parameters: $a > 0$ sets the relative time scale between voltage and recovery variable, and I and b allow bifurcations between different phase

portraits that interact with the reset parameters c and d to create a rich repertoire of spiking and bursting behaviors. Here we will call Eq. (9) the RQIF model (QIF with a recovery variable).

After reviewing the bifurcations of the RQIF model we compute its firing rates in the case that $a \ll 1$, first under the simplifying condition that post-spike solutions are reset to a specific point in the phase plane ("instantaneous rates", §3.2), and then by seeking a fixed point for an averaged system ("asymptotic rates", §3.3).

3.1 Bifurcations and phase planes of the RQIF model

Here we briefly review the dynamics of Eq. (9) for $v < v_{peak}$. Previous studies of bifurcations and phase portraits appear in (Izhikevich, 2006, Ch. 8) and (Touboul, 2008; Touboul and Brette, 2009), and the latter papers generalize the analyses to systems with strictly convex functions $F(v)$ in place of v^2.

As I decreases for $a > 0$ and b fixed, local saddle-node (SN) and Andronov-Hopf (AH) bifurcations and a global homoclinic (Hom) or saddle-loop bifurcation occur as illustrated in Figs. 3 and 4 (cf. (Guckenheimer and Holmes, 1983; Kuznetsov, 2004)):

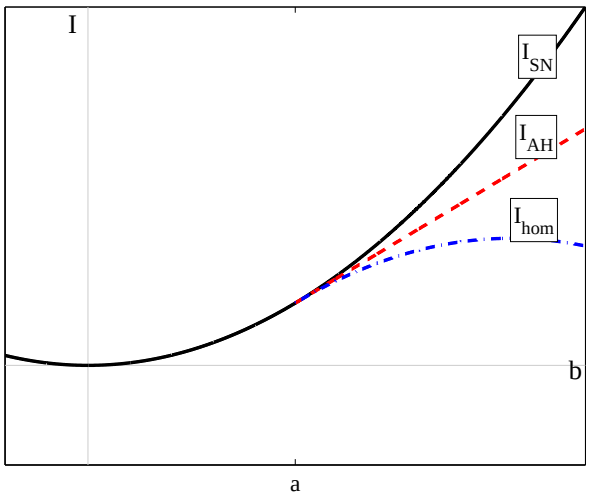

Figure 3: Bifurcation diagram in terms of the parameters I and b. Saddle node bifurcations occur on the solid curve I_{SN}, Eq. (11), Andronov-Hopf bifurcations on the dashed curve I_{AH}, Eq. (12), and homoclinic bifurcations on the dashed-dotted curve I_{hom}, Eq. (13). The curves meet with a common tangent at the Takens-Bogdanov bifurcation point $(b = a, I = a^2/4)$.

SN: Two fixed points

$$v_f^{\pm} = \frac{1}{2}(b \pm \sqrt{b^2 - 4I}),\ u_f^{\pm} = bv_f^{\pm}, \tag{10}$$

henceforth denoted v_{th} and v_{rest}, appear in a saddle-node bifurcation on the curve

$$I = I_{SN} = b^2/4; \tag{11}$$

v_{th} is a hyperbolic saddle point for all $I < I_{SN}$, v_{rest} is a sink for $b \leq a$ and appears below I_{SN} as a source for $b > a$.

AH: As $I < I_{SN}$ decreases for $b > a$, v_{rest} becomes a sink in a subcritical Andronov-Hopf bifurcation on the line

$$I = I_{AH} = \frac{ab}{2} - \frac{a^2}{4},\ b > a, \tag{12}$$

below which an unstable limit cycle appears, initially bounding the domain of attraction of the sink, hereafter denoted $W^s(v_{rest})$ and shaded gray in the phase portraits of Fig. 4.

Hom: As $I < I_{SN}$ continues to decrease, the unstable cycle grows and forms a saddle connection to v_{th} in a homoclinic bifurcation that occurs on a curve approximated by

$$I = I_{hom} = \frac{a^2}{4} + \frac{a(b-a)}{2} - \frac{6(b-a)^2}{25} + \mathcal{O}(|b-a|^3);\ b > a. \tag{13}$$

Below I_{hom} there is no limit cycle and the nonwandering set consists of v_{th} and the sink v_{rest} alone. The curves I_{SN}, I_{AH} and I_{hom} meet with common tangents at the codimension two Takens-Bogdanov bifurcation point $(b = a, I = a^2/4)$.

In the Appendix we provide details of the underlying ideas and analysis, particularly of the Takens-Bogdanov and homoclinic bifurcations. The derivation of (Touboul, 2008), which appeals to results of (Kuznetsov, 2004, §8.4) but omits the blow-up calculation, appears to contain errors in expressions for the homoclinic bifurcation curve: specifically (Touboul and Brette, 2009, Eq. (2.1)) lacks the second term of Eq. (13), linear in $(b - a)$, which is necessary for the common tangency, cf. (Guckenheimer and Holmes, 1983, Fig. 7.3.3) and (Kuznetsov, 2004, Fig. 8.8).

3.2 Instantaneous firing rates for the RQIF with $a \ll 1$

We first explore the dynamics of a constrained RQIF model (9) with initial conditions reset after each spike to $(v(t^+_{peak}) = c \geq 0, u(t^+_{peak}) \stackrel{\text{def}}{=} u_0)$. Throughout this section we set $a \ll 1$, so that the recovery dynamics are slow enough that $|\dot{u}| \ll |\dot{v}|$, except near the $\dot{v} = 0$ nullcline, computation of spike times t_{peak} for different initializations u_0 results in instantaneous firing rates defined as the inverse of the ISI or time to reach v_{peak} (cf. Eqs. (3-4), although we do not include a refractory period, since the recovery variable can represent refractory dynamics). By distinguishing between the cases $I < I_{SN}$ and $I > I_{SN}$ we focus on the effects of the parameters b and I, which determine the phase plane structures, separating them into the topologically distinct classes of Fig. 4.

Touboul (Touboul, 2009) has shown that the recovery variable u blows up along with the voltage v in the quadratic RQIF model, and that this can make solutions sensitive to the choice of v_{peak} (the cutoff/reset value). Here we take $v_{peak} = 10$: sufficiently small that $u(t)$ does not appreciably accelerate as $t \to t_{peak}$ and our assumption that $u(t)$ varies slowly is justified.

3.2.1 Case (a): $I > I_{SN}$

Above I_{SN} no fixed points exist and all solutions reach v_{peak} in finite time, leading to repetitive firing whose period depends on the reset condition $u = u_0$. To describe the instantaneous firing rates we define an effective input current

$$I' = I - u_0. \tag{14}$$

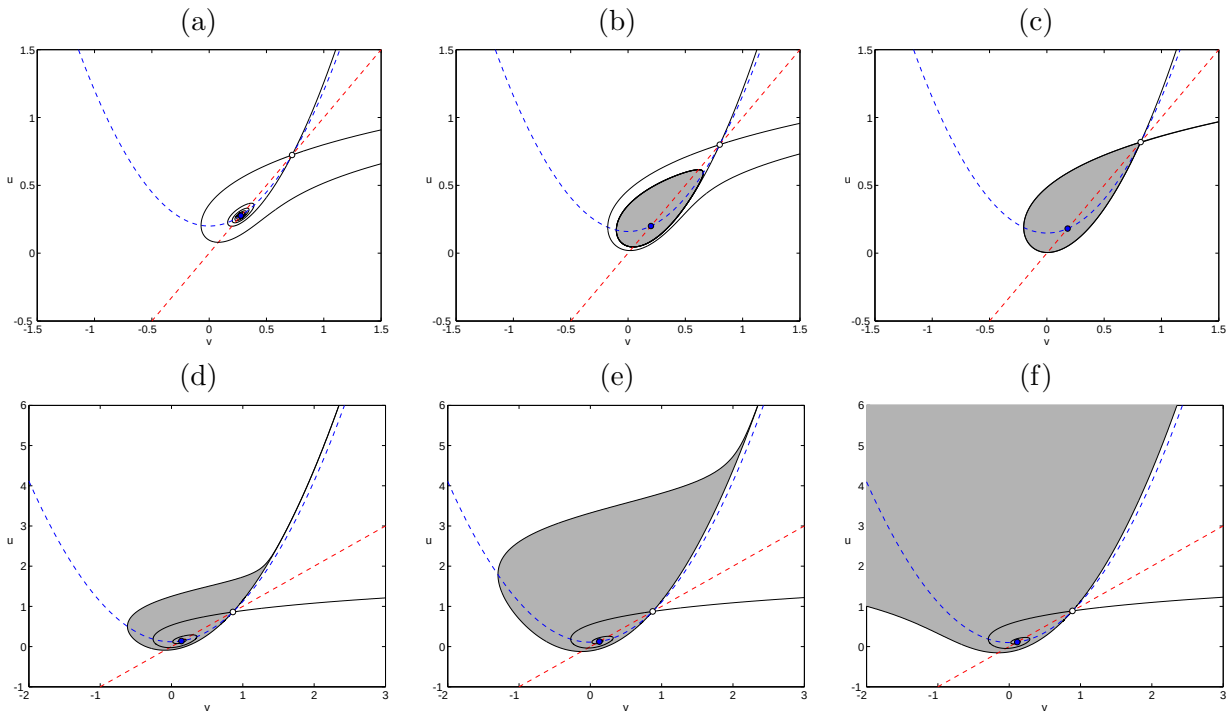

Figure 4: Phase portraits for decreasing values of $I < I_{SN}$ with $a = 0.5$, $b = 1$ fixed, showing behavior through the sequence of codimension one bifurcations, including domains of attraction (shaded) of the sink v_{rest} (filled circle) and stable and unstable manifolds $W^s(v_{th})$, $W^u(v_{th})$ of v_{th} (open circle). (a): $I_{AH} < I = 0.2 < I_{SN}$. (b): $I_{hom} < I = 0.16 < I_{AH}$, the source has undergone a Hopf bifurcation into a sink and an unstable limit cycle that bounds $W^s(v_{rest})$. (c): $I = I_{hom} \approx 0.1485$, the limit cycle fuses with $W^s(v_{th}) \cap W^u(v_{th})$, creating a homoclinic orbit. (d): $I = 0.12 < I_{hom}$, $W^s(v_{th})$ and $W^u(v_{th})$ separate to create an unbounded trapping region with a thin "tongue" extending up the right branch of the $\dot{v} = 0$ nullcline. (e): $I = 0.11 < I_{hom}$, the trapping region grows but remains of bounded width. (f): $I = 0.1 \ll I_{hom}$, the trapping region's width becomes unbounded as the left hand branch of $W^s(v_{th})$ falls outside the $\dot{v} = 0$ nullcline.

Since the extremum of the $\dot{v} = 0$ nullcline lies at $(v, u) = (0, I)$, $I' < 0$ (resp. $I' > 0$) corresponds to initial conditions above (resp. below) this nullcline, prompting our classification of firing rates into three regimes: *above threshold*: $I' > \varepsilon$, *below threshold*: $I' < -\varepsilon$, and *near threshold*: $|I'| < \varepsilon$. In the first regime, time scale separation is preserved and $u(t)$ remains almost constant ($u(t) \approx u_0$); in the second and third regimes, solutions enter an ε-neighborhood of the nullcline and cross it, timescale separation fails, and we must allow $u(t)$ to evolve; see Fig. 5. The small parameter $\varepsilon(a, I) > 0$ will be determined below.

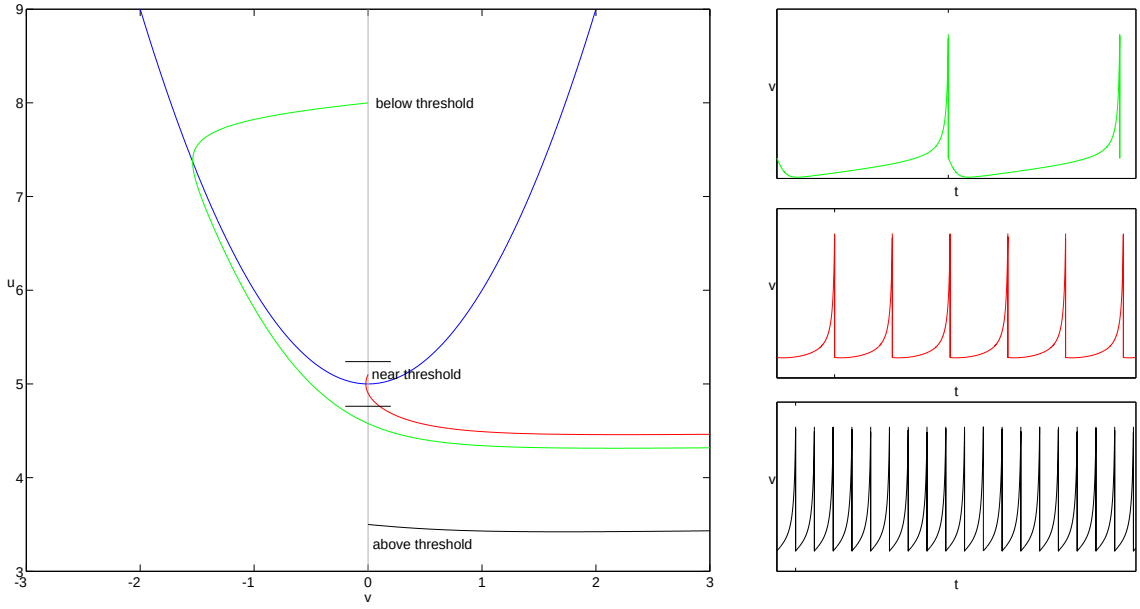

Figure 5: Below, near and above threshold escape regions (left) and corresponding spike trains (right) for $a = 0.05, b = 2, I = 5, c = 0$ and $\varepsilon = 0.2381$.

$\underline{I' > \varepsilon}$: In the above-threshold regime v increases rapidly until the solution reaches v_{peak}, while $u(t) \approx u_0$ remains almost constant. The ISI may therefore be estimated as in Eqs. (7-8):

$$T_a(I') = \frac{1}{\sqrt{I'}} \operatorname{atan}\left[\frac{\sqrt{I'}(v_{peak}-c)}{I'+cv_{peak}}\right] = \begin{cases} \frac{1}{\sqrt{I'}} \operatorname{atan}\left[\frac{\sqrt{I'}(v_{peak}-c)}{I'+cv_{peak}}\right], & I' \geq 0, \\ \frac{1}{2\sqrt{|I'|}} \ln\left[\frac{\left(v_{peak}-\sqrt{|I'|}\right)\left(c+\sqrt{|I'|}\right)}{\left(v_{peak}+\sqrt{|I'|}\right)\left(c-\sqrt{|I'|}\right)}\right], & -c^2 < I' < 0. \end{cases} \tag{15}$$

As $I' \to -c^2$ for $c \neq 0$, the instantaneous firing rate $1/T_a(I')$ is dominated by the term $2c/\ln[4\alpha c^2/(c^2+I')]$ with $\alpha = (v_{peak}-c)/(v_{peak}+c)$. This produces sharper curvature near threshold than that for $c = 0$, for which firing rates scale as $\sqrt{I'}$ as $I' \to 0$: see Figs. 6 and 9, case FS2, below.

$\underline{|I'| < \varepsilon}$: The near-threshold regime occurs when solutions are reset near the $\dot{v} = 0$ nullcline, where separation into slow and fast dynamics fails since $|\dot{v}| \approx |\dot{u}|$. For $v = c = 0$, Eq. (9) decouples and the time taken to travel from $u_0 = I - I'$ to $u = I - \varepsilon$ can be found by integrating $\dot{u} = -au$:

$$T_{th1}(I') = \frac{1}{a} \ln\left(\frac{I-I'}{I-\varepsilon}\right). \tag{16}$$

Below the nullcline's minimum v accelerates and at $\dot{v} = -\dot{u}$ we can switch to the $\dot{v}$ dynamics with $u(t) \approx u_0 = I - \varepsilon$, obtaining the same estimate as (15) with $c = 0$ and $I' = I - u_0 \geq 0$ replaced by ε. Adding this and (16) yields the near-threshold ISI:

$$T_{th}(I') = \frac{1}{\sqrt{\varepsilon}} \left[\operatorname{atan}\left(\frac{v_{peak}}{\sqrt{\varepsilon}}\right)\right] + \frac{1}{a} \ln\left(\frac{I-I'}{I-\varepsilon}\right). \tag{17}$$

The parameter ε is estimated by setting $\dot{v} = -\dot{u}$ and $v = 0$ in Eq. (9), giving $u = I/(a+1)$ at the turning point, or, in terms of I',

$$I' = I - u = \frac{aI}{1+a} \stackrel{\text{def}}{=} \varepsilon. \tag{18}$$

For resets with $v = c > 0$, the near threshold regime occurs when $I' = I - u$ lies in the interval $(-c^2, \epsilon - c^2]$. In this case the ISI is approximated by

$$T_{th}(I') = T_a(-c^2 + \epsilon) + \frac{1}{a} \ln\left(\frac{I - I' - bc}{I + c^2 - \epsilon - bc}\right), \tag{19}$$

where the second term in $T_{th}(I')$ is obtained by solving the inhomogeneous ODE $\dot{u} + au = abc$ and ϵ is estimated by setting $\dot{v} = -\dot{u}$ with $v = c$ in Eq. (9), giving

$$\epsilon \stackrel{\text{def}}{=} I + c^2 - u = \frac{a(c(c-b) + I)}{1+a}. \tag{20}$$

$\underline{I' < -\varepsilon}$: In the below-threshold regime the initial condition lies above the parabola, so solutions start with fast dynamics in v towards the left branch of the $\dot{v} = 0$ nullcline until $\dot{v} \approx \dot{u}$, with time of flight $T_{b1}(I')$. The nullcline is crossed and slow dynamics of duration $T_{b2}(I')$ then ensues along its left branch. This is followed by near-threshold dynamics at the nullcline's minimum at $v = 0, u = I$, and fast dynamics in v towards v_{peak}, with time of flight given by Eq. (17) with $I' = 0$.

The initial fast phase is estimated by integrating the $\dot{v}$ equation

$$T_{b1}(I') = \int_c^{v_\varepsilon} \frac{dv}{v^2 - |I'|} = \frac{1}{2\sqrt{|I'|}} \ln\left[\frac{\left(\sqrt{|I'|} - v_\varepsilon\right)\left(\sqrt{|I'|} + c\right)}{\left(\sqrt{|I'|} + v_\varepsilon\right)\left(\sqrt{|I'|} - c\right)}\right] \tag{21}$$

(cf. Eq. (8)), where v_ε is found by setting $\dot{v} = \dot{u}$ and $u = I - I'$ in Eq. (9), giving the quadratic equation $v^2 - abv + I'(1-a) + aI = 0$. Choosing the appropriate root, we find

$$v_\varepsilon = \frac{ab - \sqrt{a^2b^2 - 4(I'(1-a) + aI))}}{2}. \tag{22}$$

During the slow dynamics, solutions remain near the left branch of the nullcline $v_{lb} = -\sqrt{u - I}$, substitution of which in the slow equation yields $\dot{u} = -a(b\sqrt{u - I} + u)$. Integrating this ODE gives the estimate

$$T_{b2}(I') = -\frac{1}{a}\int_{u_0}^{I} \frac{du}{b\sqrt{u-I} + u} = \frac{1}{a}\left[\frac{2b}{K}\ \text{atan}\left(\frac{b - 2v_{lb}}{K}\right) - \ln(u - bv_{lb})\right]_{u_0}^{I}, \tag{23}$$

where $K = \sqrt{4I - b^2}$.

In summary, the ISI in the below-threshold regime is given by

$$T_b(I') = T_{b1}(I') + T_{b2}(I') + T_{th}(0). \tag{24}$$

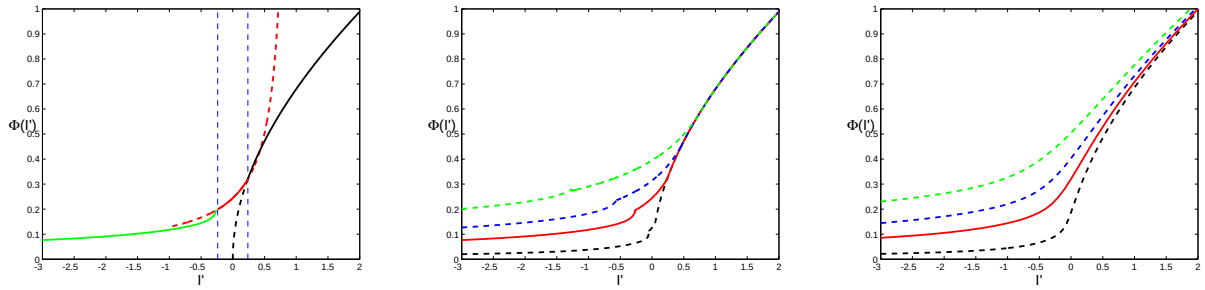

Figure 6: Instantaneous Firing rate curves for the RQIF model with $c = 0$, $b = 1$, $I = 5 > I_{SN}$ and reset $v = 0, u = u_0$. Left: Analytical estimates of firing rates for $a = 0.05$ in above-, near- and below-threshold regions (black, red and green respectively); vertical blue lines at $I' = \pm\varepsilon$ separate the regions and curves are continued (dashed) outside each region. Middle: Analytical estimates with $a = 0.2,\ 0.1,\ 0.05,\ 0.01$ (top to bottom). Right: Firing rates derived from numerical simulation of Eq. (9) with $a = 0.2,\ 0.1,\ 0.05,\ 0.01$ (top to bottom).

Firing rate curves $\Phi(I')$ defined by Eqs. (15), (17-18) and (21-24) are illustrated in Fig. 6 for $c = 0$ and four values of a, in comparison with the results of direct simulations. Note the close agreement, even for $a = 0.2$, and the growth of the near-threshold regime with a (Eq. (18)). While similar to that of the QIF above threshold ($I' > \varepsilon$, cf. Fig. 1), the curvature of $\Phi(I')$ changes sign near threshold, and firing rates remain finite below threshold ($I' < -\varepsilon$). Here the slow dynamics of the recovery variable dominates the ISI via the component $T_{b2}(I')$ in $T_b(I')$, producing firing rates that gradually decrease with I'. This provides a deterministic mechanism for subthreshold firing, in contrast to stochastic input currents in the LIF and QIF models (Wan and Tuckwell, 1982; Amit and Tsodyks, 1991). Furthermore, as c increases the above-threshold ISI decreases while the below-threshold ISI increases, producing a sharp drop in instantaneous firing rates from above ($I' > -c^2$) to below threshold ($I' < -c^2$), cf. Fig. 9, case FS2, below. This change in firing rates is responsible for initial or sustained bursts when $d > 0$, see §§3.3 and 4.1 and Fig. 11 below for explanation.

3.2.2 Case (b): $I < I_{SN}$

For $I < I_{SN}$ the two fixed points exist, but if solutions are reset with $c = 0$ and $u_0 < I$ sufficiently far below the $\dot{v} = 0$ nullcline, the initial condition lies below the stable manifold $W^s(v_{th})$ of the saddle point (cf. Fig. 4). Consequently it cannot be captured by the second fixed point v_{rest}, even if v_{rest} is stable, and repetitive firing occurs much as in the above-threshold case and the ISI is approximated by Eq. (15).

When v_{rest} is a stable sink and the left hand branch of $W^s(v_{th})$ lies below the $\dot{v} = 0$ nullcline (e.g. Fig. 4(f)), initial conditions above this nullcline are attracted rapidly to its left branch and thereafter converge slowly to v_{rest}. The system is excitable, but no periodic firing occurs. However, this is only one aspect of the rich dynamics implicit in the codimension two, AH and homoclinic bifurcations analyzed in §§3.1 and the Appendix. In Fig. 7 we show firing rate curves corresponding to the analogous panels (a-f) of Fig. 4. As already noted, the location of the reset point relative to $W^s(v_{th})$ is a key factor in determining the fate of solutions and hence firing rates when repetitive spiking occurs, but the unstable limit cycle and homoclinic loop, when they exist, bound $W^s(v_{rest})$,

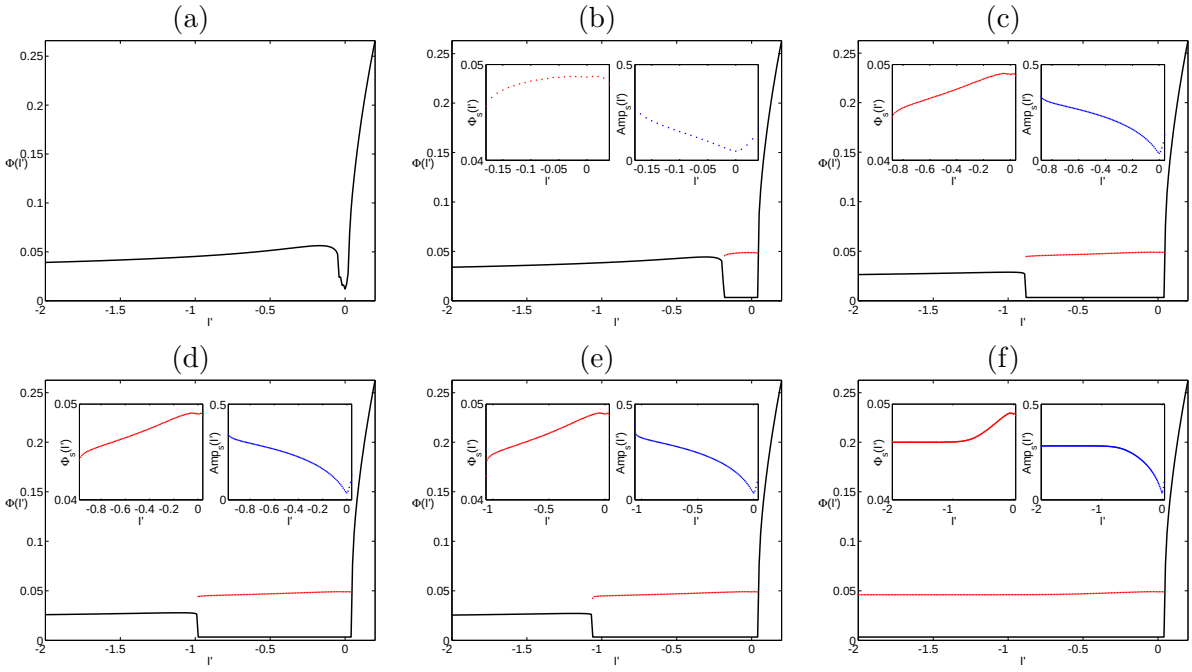

Figure 7: Firing rate curves (solid black) for parameter values corresponding to the phase planes of Fig. 4 with $I < I_{SN}$: $a = 0.1, c = 0, b = 1$ and $I = 0.059, 0.03, 0.02438, 0.024377, 0.024376, 0.02435$ (a-f). Firing rates (red) and amplitudes (blue) of subthreshold oscillations are enlarged in insets. See text for details.

leading to different behaviors as I and b range over the parameter space of Fig. 3.

We start with (b, I) in the region of Fig. 3 below I_{SN} and above I_{AH}. Here v_{rest} is a source whose unstable manifold contains the left hand branch of $W^s(v_{th})$ and all initial conditions except those in $W^s(v_{th})$ (a set of measure zero) escape to v_{peak}: Fig. 4(a). Solutions starting outside the "tongue" bounded by the unstable manifold $W^u(v_{th})$ behave much as in case (a), escaping directly for u_0 below $W^u(v_{th})$ (as for Eq. (15)), and for u_0 above $W^u(v_{th})$, traveling leftward, crossing the left branch of the $\dot{v} = 0$ nullcline, turning and then escaping. Solutions starting inside the tongue sufficiently close to $W^u(v_{th})$ behave similarly, but when the source is a focus, solutions starting near it can exhibit prolonged growing subthreshold oscillations followed by slow passage near v_{th} prior to escape. Firing rates for I' above and below threshold are therefore similar to those in case (a), but as I' decreases and reset points move upward, $\Phi(I')$ drops rapidly toward zero before recovering as u_0 enters and leaves a neighborhood of v_{rest}: Fig. 7(a).

Below I_{AH} v_{rest} is a sink, which is surrounded by an unstable limit cycle that tends to a homoclinic loop as (b, I) approaches I_{hom}: Figs. 4(b,c). The cycle bounds the sink's domain of attraction $W^s(v_{rest})$, so that solutions started inside it exhibit decaying subthreshold oscillations as they converge on v_{rest}. Solutions reset outside the cycle continue to behave like those for (b, I) between I_{SN} and I_{AH} and in case (a), but for I' such that u_0 lies in $W^s(v_{rest})$ the firing rate is zero: Fig. 7(b). On this and subsequent panels we also indicate the frequency of the subthreshold oscillations in red, enlarged in the left inset along with their amplitudes in the right inset; frequency and amplitudes are computed by averaging over first three cycles after reset.

As (b, I) approaches I_{hom} the limit cycle grows, thereby enlarging the interval in I' for which $\Phi(I') = 0$, and on I_{hom} the decaying oscillations start with near zero frequency when reset near the homoclinic loop $(W^u(v_{th}) \cap W^s(v_{th}))$, and approach the frequency of the system linearized at v_{rest} as time proceeds, producing the firing rate and amplitude curves of Fig. 7(c).

For (b, I) below I_{hom} $W^u(v_{th})$ and $W^s(v_{th})$ separate and $W^s(v_{th})$ now bounds $W^s(v_{rest})$, which resembles a teardrop hanging by a thread along the right branch of the $\dot{v} = 0$ nullcline, to which both branches of $W^s(v_{th})$ asymptote: Figs. 4(d,e). As I decreases the teardrop grows and finally "breaks" as the left hand branch of $W^s(v_{th})$ passes outside the parabolic nullcline and the domain of attraction of v_{rest} grows to include all initial conditions above $\dot{v} = 0$, as in Fig. 4(f). The interval over which $\Phi(I') = 0$ increases and the frequency of the decaying subthreshold oscillations that exist in this region settles on that of the system linearized at v_{rest}: see Figs. 7(d), (e) and (f).

For larger values of a, such as that of Fig. 4, the region inside $W^s(v_{th})$ grows, resulting in larger ranges in which $\Phi(I') = 0$.

For $0 < c < v_{th}$ we expect instantaneous firing rate curves to have similar features as for $c = 0$, with the interval in which $\Phi(I') = 0$ determined by the intersection of the line $v_0 = c$ with $W^s(v_{rest})$. For $c > v_{th}$ the curve in the above threshold regime is replaced by the second expression of Eq. (15) up to intersection with the stable manifold $W^s(v_{th})$, at which $\Phi(I') = 0$. The near- and below-threshold regimes are similar to Fig. 7: for $I_{hom} < I < I_{SN}$, $\Phi(I')$ recovers rapidly from dropping to zero exhibiting below threshold firing rate (as in Fig. 7(a)). For $I < I_{hom}$, $\Phi(I')$ can have a range of $\Phi(I') = 0$ determined by two intersections of the line $v_0 = c$ with $W^s(v_{th})$ (Figs. 7(d,e)) and an unbounded range in which $\Phi(I') = 0$ when there is only one intersection (Fig. 7(f)).

3.3 Asymptotic firing rates for the RQIF with $a \ll 1$

We now allow the recovery variable $u(t)$ to evolve, and predict asymptotic firing rates $\Phi(I)$ by using the ISIs T_a, T_{th} and T_b estimated in §3.2.1 along with averaging theory (Sanders et al., 2007), (Guckenheimer and Holmes, 1983, §4.1) to determine the asymptotic dynamics of $u(t)$ as $t \to \infty$. Stable fixed points of the averaged system provide self-consistent estimates of reset conditions that can replace u_0 in the formulae of §3.2. We start with $c = d = 0$ before generalizing to $d \neq 0$ and $v_{peak} > c > 0$.

3.3.1 Case (a): $I > I_{SN}$

Rewriting Eq. (9) as a regular perturbation problem

$$\dot{x} = \begin{pmatrix} \dot{v} \\ \dot{u} \end{pmatrix} = \begin{pmatrix} v^2 + I - u \\ 0 \end{pmatrix} + a \begin{pmatrix} 0 \\ bv - u \end{pmatrix} \stackrel{\text{def}}{=} f(x) + ag(x);\ a \ll 1, \tag{25}$$

and following (Sanders et al., 2007, §1.6), we use the exact solution $z(\zeta, t)$ for $a = 0$, where ζ denotes the initial conditions, to put (25) into standard form for averaging with uniformly small right hand side:

$$\dot{\zeta} = a \left[D_\zeta z(\zeta, t) \right]^{-1} g(\zeta, t). \tag{26}$$

For $I > I_{SN}$ the unperturbed solution is given by

$$z(\zeta, t) = \begin{pmatrix} \zeta_1 + \sqrt{I - \zeta_2} \tan\left(t\sqrt{I - \zeta_2}\right) \\ \zeta_2 \end{pmatrix} \ \Rightarrow\ D_\zeta z(\zeta, t) = \begin{bmatrix} 1 & p(\zeta_2, t) \\ 0 & 1 \end{bmatrix}, \tag{27}$$

where $p(\zeta_2, t) = \partial z_1(\zeta, t)/\partial \zeta_2$ will not be needed in evaluating the second row of Eq. (26).

Case of $c = 0$: Setting $\zeta_1 = v(0) = 0$, the second row of Eq. (26) becomes

$$\dot{\zeta}_2 = a[b\sqrt{I - \zeta_2}\tan(t\sqrt{I - \zeta_2}) - \zeta_2] \tag{28}$$

The relevant solution of Eq. (25) with $d = 0$ and $(v(t^+_{peak}) = c = 0,\ u(t^+_{peak}) = \zeta_2)$ is periodic with period

$$T_a(I - \zeta_2) = \frac{1}{\sqrt{I - \zeta_2}}\text{atan}\left(\frac{v_{peak}}{\sqrt{I - \zeta_2}}\right) \tag{29}$$

(cf. case $I' \geq 0$ of Eq. (15)), so we may compute the averaged ODE corresponding to Eq. (28):

$$\dot{\bar{\zeta}}_2 = \frac{a}{T_a}\int_0^{T_a} [b\sqrt{I - \zeta_2}\tan(t\sqrt{I - \zeta_2}) - \zeta_2]\, dt \stackrel{\text{def}}{=} a[\bar{h}_2(\bar{\zeta}_2) - \bar{\zeta}_2], \tag{30}$$

$$\text{where}\ \ \bar{h}_2(\bar{\zeta}_2) = \frac{b\sqrt{I - \bar{\zeta}_2}\,\ln\left[1 + v^2_{peak}/(I - \bar{\zeta}_2)\right]}{2\ \text{atan}\left[v_{peak}/\sqrt{I - \bar{\zeta}_2}\right]}. \tag{31}$$

We now appeal to the averaging theorem to assert that solutions of Eq. (28) and of the averaged ODE (30) remain within $\mathcal{O}(a)$ on a timescale of $\mathcal{O}(1/a)$. In particular, when Eq. (30) has a stable hyperbolic fixed point $\bar{\zeta}_2^{fp}$, orbits of Eq. (26), and hence also of Eq. (25), will approach a periodic orbit of period $T_a(I - \bar{\zeta}_2^{fp})$ that lies within $\mathcal{O}(a)$ of $u = \bar{\zeta}_2^{fp}$. The asymptotic firing rate is therefore given by $\Phi(I) = 1/T_a(I - \bar{\zeta}_2^{fp})$, leading to the curve labeled $d = 0$ in the left panel of Fig. 8.

To prove that there is a unique stable hyperbolic fixed point, it suffices to show that the range of $\bar{h}_2(\bar{\zeta}_2)$ is $[0, k]$ for some $k > 0$ and that its derivative is negative, implying that the equation $\bar{h}_2(\bar{\zeta}_2) = \bar{\zeta}_2$ has a unique solution $\bar{\zeta}_2^{fp}$ at which $\bar{h}_2'(\bar{\zeta}_2^{fp}) - 1 < 0$. This is done in the Appendix.

For $d \neq 0$ the slow evolution of $\bar{\zeta}_2$ is followed by a discrete jump. To compute the effective value of $\bar{\zeta}_2$ it seems simplest to approximate the solution of the averaged equation (30) at $t = T_a$ by a single step of Euler's method, which, like Eq. (30), is accurate to $\mathcal{O}(a)$, and augment by d:

$$\bar{\zeta}_2(T_a^+) = \bar{\zeta}_2(0) + aq(\bar{\zeta}_2(0)) + d,\ \text{where}\ \ q(\bar{\zeta}_2(0)) = [\bar{h}_2(\bar{\zeta}_2(0)) - \bar{\zeta}_2(0)]T_a(I - \bar{\zeta}_2(0)). \tag{32}$$

The fixed point, which provides an estimate of the reset point $u(t^-_{peak}) + d$, satisfies $q(\bar{\zeta}_2^{fp}) = -d/a$. Values of the function $q(\bar{\zeta}_2)$ with domain $(-\infty, I]$ limit on v_{peak} as $\bar{\zeta}_2 \to -\infty$ and on $-\infty$ as $\bar{\zeta}_2 \to I$. Fixed points therefore exist for $d > -av_{peak}$; moreover, in the Appendix they are proved to be unique for all $d \geq 0$ and for $d < 0$ with $|d|$ sufficiently small. Numerical evaluations suggest uniqueness for all $d > -av_{peak}$: see the left panel of Fig. 16 below.

Examples of firing rate curves for $d \neq 0$ are given in the left panel of Fig. 8, in comparison with those for the QIF without a refractory period. Note that the curves also depend on a, unlike in the case $d = 0$. For $d < 0$, the RQIF firing rate curves intersect the QIF curve or lie below it for all $I > I_{SN}$. For $d < -av_{peak}$ there is no fixed point, and $I - \bar{\zeta}_2$ increases and blows up along the above-threshold instantaneous firing rate curve. Asymptotic firing rates are not defined for any choice of I in this regime.

For $d \geq 0$, where the fixed point always exists, increasing d brings $\bar{\zeta}_2^{fp}$ closer to I from below and causes the firing rate curve to become almost linear: a phenomenon observed in experiments

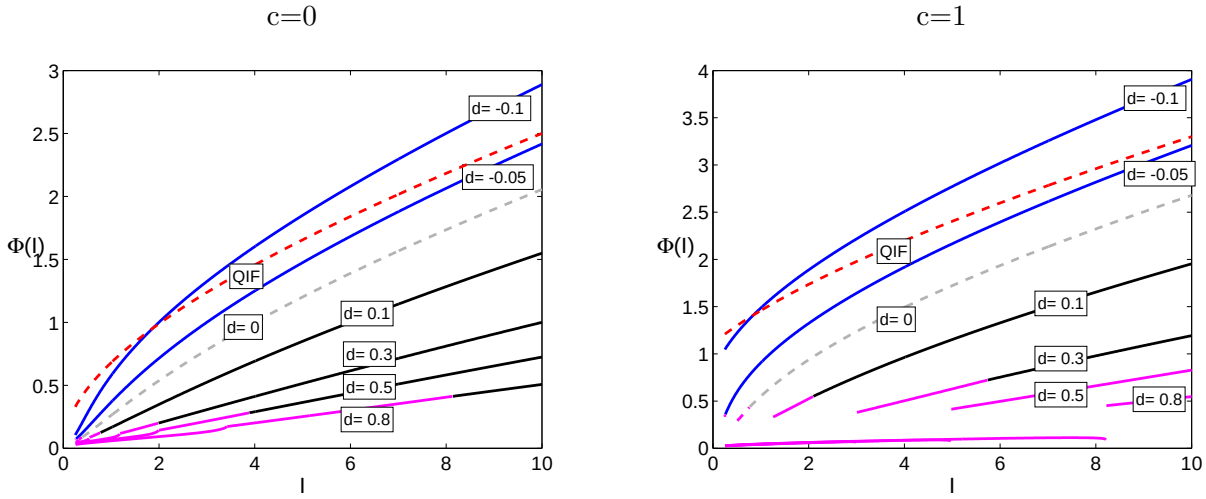

Figure 8: Estimates of asymptotic firing rates for the RQIF model with $I > I_{SN}$ and $a = 0.05, b = 1$ for $c = 0$ (left) and $c = 1$ (right). Firing rates of the QIF model without refractory period (dashed red) lie above those of the RQIF model with $d = 0$ (gray) and $d = 0.1, 0.3, 0.5, 0.8$ (solid black); for negative $d = -0.05, -0.1$ (solid blue) they can exceed those of QIF. As I decreases, near-threshold firing rates (magenta) for $c = 0$ and $d > 0$ transition continuously to below-threshold firing rates while for $c = 1$ and $d > 0$ they transition to bursting, producing a discontinuous jump to a curve that describes bursting rates. See text for further information.

with adaptation (McCormick et al., 1985) and explained using linear approximation of the averaged equations in (Ermentrout, 1998). As $\bar{\zeta}_2^{fp}$ approaches I, it eventually enters the near-threshold region; where the flight time changes from T_a to T_{th}, the asymptotic periodic orbit departs for v_{peak} from the near-threshold region, and the curves in Fig. 8 change from black to magenta. The system therefore settles on periodic firing with resets at $v = 0$ and $u = u(t^+_{peak})$, which may be estimated by computing the first iterate, $\bar{\zeta}_2(T_{th})$, of the map (32), initiated at the exit point from the near-threshold regime: $\bar{\zeta}_2(0) = I - \varepsilon$. Firing rates are then computed from $1/T_{th}(I - \bar{\zeta}_2(T_{th}))$ when $\bar{\zeta}_2(T_{th})$ lies in the near-threshold region and $1/T_b(I - \bar{\zeta}_2(T_{th}))$ when it lies in the below-threshold region.

Case of $c > 0$: For $v(0) = c > 0$, the first component of the unperturbed solution of Eq. (25) is

$$\zeta_1(t) = \sqrt{I - \zeta_2}\tan\left[t\sqrt{I - \zeta_2} + \text{atan}\left(\frac{c}{\sqrt{I - \zeta_2}}\right)\right], \tag{33}$$

which results in an ODE similar to Eq. (28) with an extra term:

$$\dot{\zeta}_2 = a\left(b\sqrt{I - \zeta_2}\tan\left[t\sqrt{I - \zeta_2} + \text{atan}\left(\frac{c}{\sqrt{I - \zeta_2}}\right)\right] - \zeta_2\right). \tag{34}$$

Replacing $T_a(I - \zeta_2)$ in Eq. (29) by the appropriate expression from Eq. (15):

$$T_a(I - \zeta_2) = \frac{1}{\sqrt{I - \zeta_2}}\text{atan}\left[\frac{(v_{peak} - c)\sqrt{I - \zeta_2}}{cv_{peak} + I - \zeta_2}\right], \tag{35}$$

the averaged equation for $\bar{\zeta}_2$ becomes

$$\dot{\bar{\zeta}}_2 = a[\bar{h}_2(\bar{\zeta}_2)_{c>0} - \bar{\zeta}_2], \text{ where } \bar{h}_2(\bar{\zeta}_2)_{c>0} = -\frac{b}{T_a}\ln\left(\cos\left[t\sqrt{I-\bar{\zeta}_2} + \text{atan}\left(\frac{c}{\sqrt{I-\bar{\zeta}_2}}\right)\right]\right)\Bigg|_0^{T_a}$$
$$= \frac{b\sqrt{I-\bar{\zeta}_2}\,\ln\left[\frac{v_{peak}^2+I-\bar{\zeta}_2}{c^2+I-\bar{\zeta}_2}\right]}{2\ \text{atan}\left[\frac{(v_{peak}-c)\sqrt{I-\bar{\zeta}_2}}{cv_{peak}+I-\bar{\zeta}_2}\right]} = \frac{b\sqrt{\bar{\zeta}_2-I}\ln\left[\frac{v_{peak}^2+I-\bar{\zeta}_2}{c^2+I-\bar{\zeta}_2}\right]}{2\ \text{atanh}\left[\frac{(v_{peak}-c)\sqrt{\bar{\zeta}_2-I}}{cv_{peak}+I-\bar{\zeta}_2}\right]}. \tag{36}$$

Note that, while both its numerator and denominator pass through 0 and become imaginary as ζ_2 increases through I, $\bar{h}_2(\bar{\zeta}_2)_{c>0}$ is well-defined for all $\bar{\zeta}_2 \in (-\infty, I+c^2)$. We give real expressions for $\bar{\zeta}_2 < I$ and $\bar{\zeta}_2 > I$ in Eq. (36), both of which reduce to Eq. (30) for $c = 0$. Like (30), Eq. (36) also has a unique stable hyperbolic fixed point, as shown in the Appendix.

For $d \neq 0$ the averaged flow can be approximated by a one-step Euler map, as in Eq. (32):

$$\bar{\zeta}_2(T_a^+) = \bar{\zeta}_2(0) + a[h_2(\bar{\zeta}_2(0))_{c>0} - \bar{\zeta}_2(0)]T_a = -d/a, \tag{37}$$

resulting in an analogous equation for the fixed point $\bar{\zeta}_2^{fp}$,

$$q(\bar{\zeta}_2^{fp})_{c>0} = [h_2(\bar{\zeta}_2^{fp})_{c>0} - \bar{\zeta}_2^{fp}]T_a(I - \bar{\zeta}_2^{fp}) = -d/a, \tag{38}$$

as illustrated on the right hand panel of Fig. 16 in the Appendix. Specifically, values of the function $q(\bar{\zeta}_2)_{c>0}$ with domain $(-\infty, I+c^2]$ limit on $v_{peak} - c$ as $\bar{\zeta}_2 \to -\infty$ and on $-\infty$ as $\bar{\zeta}_2 \to I + c^2$ and fixed points exist for $d > -a(v_{peak} - c)$.

As in the case $c = 0$, Eq. (37) provides estimates of firing rates in the above-threshold regime. As I decreases, periodic orbits corresponding to the fixed point of Eq. (38) approach the $\dot{v}$ nullcline and enter the near-threshold region. One iterate of the map (37), initialized at $\bar{\zeta}_2(0) = I + c^2 - \epsilon$, yields the approximate reset point $\bar{\zeta}_2(T_{th})$. If $\bar{\zeta}_2(T_{th})$ lies below the $\dot{v}$ nullcline, the asymptotic firing rate is $1/T_{th}(I - \bar{\zeta}_2(T_{th}))$; if it lies above, the orbit moves to the left-hand branch of the nullcline and exhibits slow (below-threshold) evolution.

Transitions from the near-threshold to the below-threshold regime are signalled by discontinuities of the magenta curves in Fig. 8 (right). The below-threshold orbit terminates at $v(t_{peak}^-) = v_{peak}$ and $u(t_{peak}^-) = I - \varepsilon$ and resets to $v(t_{peak}^+) = c$ and $u(t_{peak}^+) = u(t_{peak}^-) + d$. If $u(t_{peak}^+) < I + c^2$, i.e. $d < c^2 + \varepsilon$, they start to the right of the $\dot{v} = 0$ nullcline, exhibiting fast flights to v_{peak}, and, with each reset, a gradual climb towards the nullcline until $u(t_{peak}^+) > I + c^2$ and below-threshold dynamics are repeated. This produces a burst of above-threshold spikes followed by a refractory period (cf. Fig. 11 in §4 below). Bursting rates (inverses of interburst times) are estimated from $1/T_b(I - \bar{\zeta}_2(T_{th}))$ and are depicted in Fig. 8 (right), as the lowest set of magenta curves; For these low firing rates the curves are indistinguishable.

3.3.2 Case (b): $I < I_{SN}$

For $c = 0$ and $d > 0$ the computations in 3.3.1 indicate that the relevant regimes for asymptotic behavior are near- and below-threshold, cf. Fig. 8 (left). However, as described in §3.2.2, the dynamics do not always produce periodic behavior. As I decreases for fixed a and b, the area of $W^s(v_{rest})$ grows, the asymptotic orbit is eventually trapped, and typical asymptotic firing rate

curves exhibit drops to zero firing rate (cf. Figs. 4 and 7). For examples and further discussion see Figs. 12 and 13 and their description in §4 below. Also, for $c > 0$ or $d < 0$ the firing curve may include an above-threshold segment; when the fixed point of the one-step map exists and lies in the above-threshold region.

4 Modeling neural dynamics with the RQIF

Intracellular recordings reveal that cortical neurons can be classified into distinct functional types depending on their spiking and bursting patterns (Connors and Gutnick, 1990; Gray and McCormick, 1996). With sufficiently large tonic current injection, excitatory neurons exhibit *Regular Spiking* (RS), *Intrinsic Bursting* (IB) and *Chattering* (CH); while inhibitory neurons can be classified as *Fast Spiking* (FS) and *Low Threshold Spiking* (LTS). In (Izhikevich, 2003) and (Izhikevich, 2006, Ch. 8) it was shown that, given suitable parameter choices, and possibly a more general quadratic function, the RQIF model can reproduce many such patterns, as well as responses of resonator (RZ) neurons and thalamo-cortical neurons subject to hyperpolarized (negative) and brief DC-current injection.

Here we classify each cell type by setting the current I and parameters a and b to give an appropriate phase plane, and choosing reset parameters c and d that yield hybrid orbits, and hence spiking patterns, characteristic of the cell's function. We explain both the transient and asymptotic dynamics in terms of the phase plane geometry of Fig. 4, and parameter selection is guided by the bifurcation analyses of §3.1 and the instantaneous and asymptotic firing rate calculations of §§3.2-3.3. We divide the material into two subsections corresponding to cases (a) and (b) of §§3.2.1-3.2.2 and §§3.3.1-3.3.2.

4.1 Case (a): $I > I_{SN}$

Throughout this subsection we assume that $I(0) = 0$ and that $I(t)$ jumps to a value $I_{in}(t) > I_{SN}$ at some time $t^* > 0$ (stepped direct current injection):

$$I(t) = \begin{cases} 0, & \text{if } t < t^*, \\ I_{in}, & \text{if } t > t^*. \end{cases} \tag{39}$$

As long as $I(t) \equiv 0$ Eq. (9) has a stable sink at $(u, v) = (0, 0)$ and a saddle at (b, b^2), so that, if sufficient time elapses before t^*, the state will settle near $(0, 0)$, providing an initial condition at $t = t^*$ for the system with the phase plane corresponding to $I = I_{in}$.

Besides displaying time series of the resulting voltage and the refractory variables along with projections onto the phase plane, in Figs. 9-11 we also show firing rates $1/t_{peak}$ vs. $I' = I - u(t^+_{peak})$, where t_{peak} is the time from post-spike reset ($t^+_{peak,i}$) to next reset ($t^-_{peak,i+1}$) derived from simulations. These projections, along with the instantaneous firing rate curves from §§3.2-3.3, reveal how firing rates evolve and relate the classification of neural responses to the classification of dynamics in §§3.2-3.3.

Fast Spiking (FS) and Low Threshold Spiking (LTS): These responses are typical of inhibitory cortical neurons with high firing rates. Spike frequency remains almost constant in FS, but for LTS there is noticeable frequency adaptation as firing rates decrease toward an asymptote

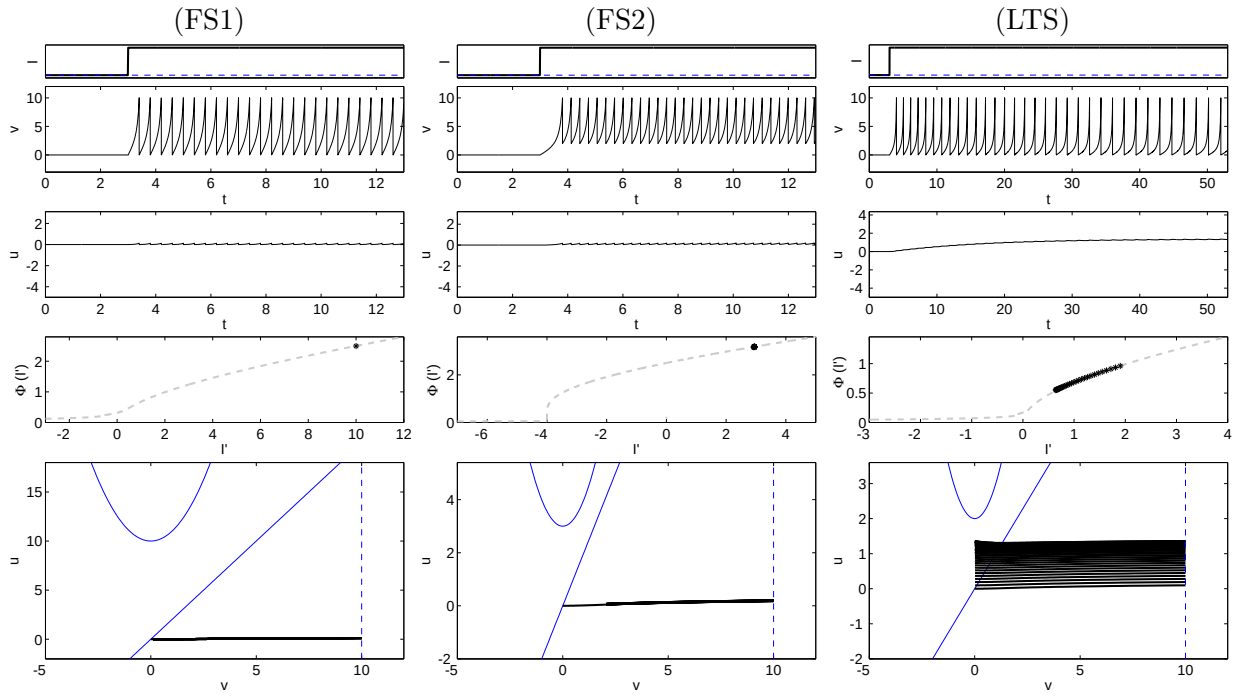

Figure 9: FS and LTS dynamics showing input current, voltage and recovery variable time series (top, second and third rows), projections onto the instantaneous firing rate curve (fourth row), and phase planes after application of I_{in} (bottom). FS1: $I_{in} = 10$, $d = -0.1194$, $c = 0$: fast spiking with no adaptation and reset to $v = 0$. FS2: $I_{in} = 3$, $d = -0.1324$, $c = 2$: fast spiking with no effective adaptation, reset point falls on first spike trajectory. LTS: $I_{in} = 2$, $d = 0$, $c = 0$: fast spiking with adaptation. Parameter $a = 0.05$ throughout, $b = 2$ for FS1 and FS2, $b = 1$ for LTS.

that depends on I_{in}. Recalling §3.2.1, we see that this behavior corresponds to the above-threshold regime in which firing rates depend sensitively on $I' = I_{in} - u_0$ such that u slowly evolves from its initial value $u_0 = 0$, to the stable fixed point of the map (32) or (37), depending on the parameters c and d.

No such evolution occurs in the left and center columns of Fig. 9: in FS1, with $c = 0$, $d < 0$ is chosen to set the fixed point $\bar{\zeta}_2^{fp} = u_0$ at the initial condition by solving the equation $q(u_0) = -d/a$ for d. This choice compensates for the increase in $u(t)$ as the orbit travels to v_{peak}, so that the state is reset near $v = u = 0$ after each spike. In FS2, we fix $c > 0$ and choose $d < 0$ by solving $q(u_0)_{c>0} = -d/a$. In both cases firing rates remains constant at $1/T_a(I - u_0)$, as depicted by a single black dot in the fourth row of the left and center columns (we start at the fixed point of the averaged equation). In contrast, for LTS (right) $c = d = 0$, the initial data produces transient dynamics that converge to the fixed point. Reset points climb the u-axis at $v_0 = 0$ until the change in $u(t)$ during evolution to v_{peak} balances to zero, while the spike frequency slides down the instantaneous firing rate curve to its asymptote $1/T_a(I - \bar{\zeta}_2^{fp})$. In all cases the averaged equation or one-step map has a stable fixed point and orbits remain in the above-threshold regime $I' > \varepsilon$.

Regular Spiking (RS): The most common response of excitatory cortical neurons to step

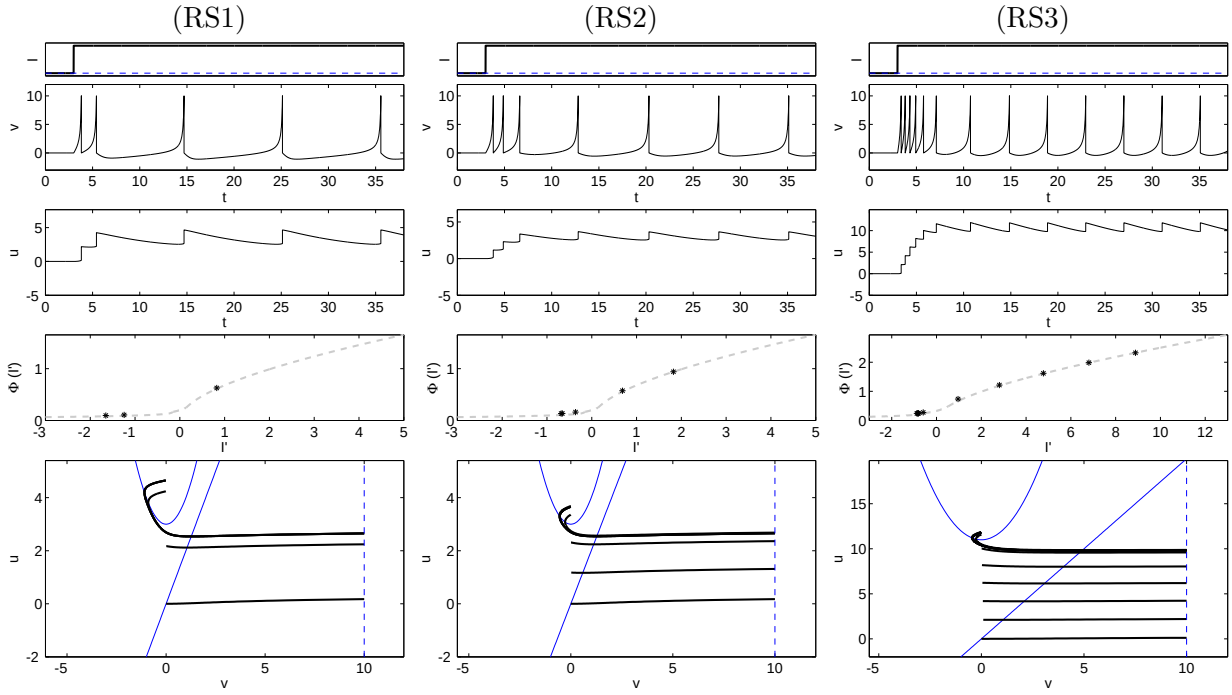

Figure 10: RS dynamics; same format as Figs. 9. RS1: $I_{in} = 3,\ d = 2$: RS with a short initial burst. RS2: $I_{in} = 3,\ d = 1$: RS with a longer initial burst due to decreased d. RS3: $I_{in} = 11,\ d = 2$: RS with a long initial burst due to increased I_{in}. Parameters $a = 0.05,\ b = 2,\ c = 0$ throughout.

current injection is a brief volley of spikes with short ISIs followed by much slower (adapted) periodic spiking. Such responses correspond to rapid transitions from above-threshold to the near- or below-threshold regimes, which can be produced by setting $c = 0$ and $d > 0$ and choosing other parameters to place the fixed point of the averaged equation or one-step map in the near-threshold regime. The transient dynamics result in positive increments in u after each reset until the near-threshold regime is reached, see §3.3.1. Subsequently, periodic spiking occurs with each ISI initiated at the first iterate, $\bar{\zeta}_2(T_{th})$, of the map (30) with initial condition $\bar{\zeta}_2(0) = I - \varepsilon$. ISIs are computed from $T_{th}(I - \bar{\zeta}_2(T_{th}))$ when $\bar{\zeta}_2(T_{th}) < I + \varepsilon$ and from $T_b(I - \bar{\zeta}_2(T_{th}))$ when $\bar{\zeta}_2(T_{th}) > I + \varepsilon$, see §3.2.1.

Some variants are shown in Fig. 10. Computation of asymptotic firing rates (cf. Fig. 8) again guides choices of c, d and I that yield the different asymptotic behaviors. For larger values of d, orbits settle to slow, below-threshold, spiking (left panel, RS1). For smaller d, reset occurs near threshold (center, RS2), and for larger I_{in} more resets are required for the orbit to equilibrate in the near-threshold region (right, RS3). The instantaneous firing rates (Fig. 10, fourth row) show transitions from above- to near- and below-threshold regimes, the number of transient spikes, and their instantaneous frequencies.

Note that, although the transition to slower periodic spiking is called adaptation in both FS and RS, the mechanisms differ: in FS, the solution settles to above-threshold periodic spiking (Fig. 9), while in RS it settles to periodic spiking in the near- or below-threshold regimes (Fig. 10). Periods in RS are therefore much longer than in FS and the initial burst and subsequent periodic spiking

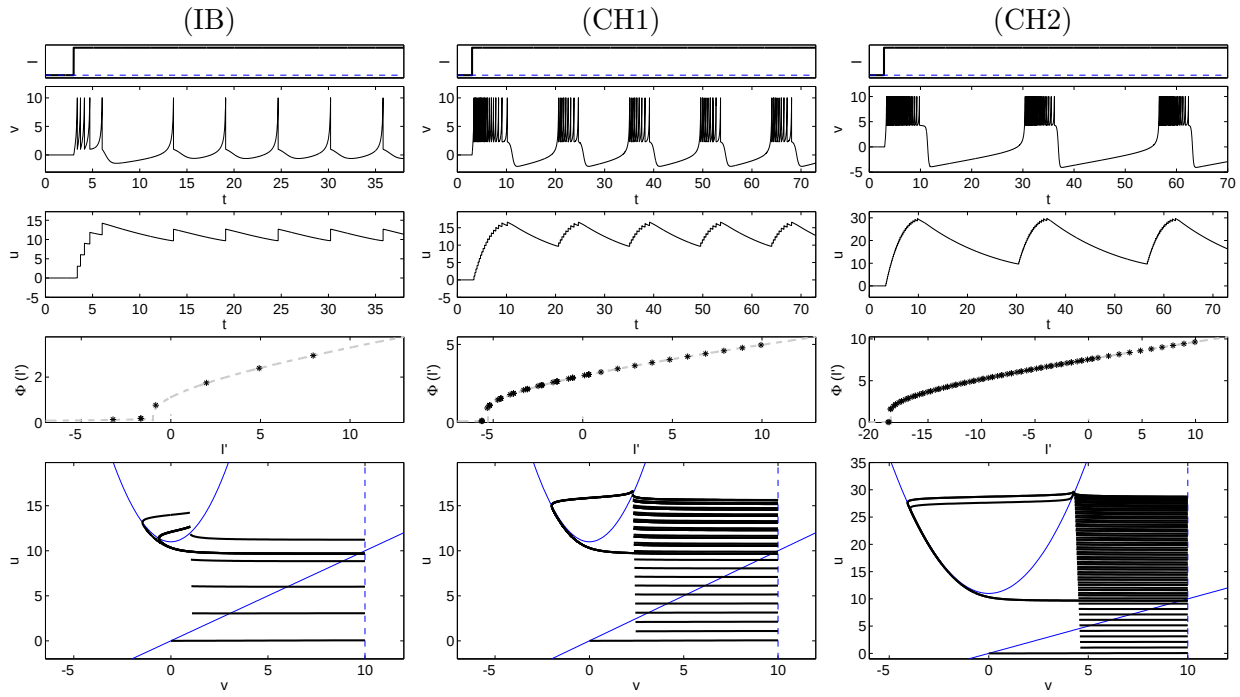

Figure 11: Typical IB and CH responses; same format as Figs. 9-10. IB: $d = 3,\ c = 1$: intrinsic bursting. CH1: $d = 1,\ c = 2.3$: chattering with short interburst intervals. CH2: $d = 2,\ c = 4.3$: chattering with more spikes in each burst and longer interburst intervals. Parameters $a = 0.05,\ b = 1,\ I_{in} = 11$ throughout.

are clearly separated.

Intrinsic Bursting (IB) and Chattering (CH): For $c > 0$ post-spike resets lie to the right of the minimum of the $\dot{v} = 0$ nullcline, closer to v_{peak}, and if $d > 0$ is sufficiently large, the dynamics settles to periodic below-threshold resets, producing either periodic spiking or bursting, as described in §3.3.1. In both cases trajectories starting above the $\dot{v} = 0$ nullcline exhibit long refractory periods before passing below its minimum and reaching v_{peak}. If $u(t^+_{peak}) > I + c^2$, each spike is followed by reset below threshold, producing periodic spiking much as in RS (Fig. 11 left, IB, cf. Fig. 10), while if $u(t^+_{peak}) \ll I + c^2$, a burst of spikes occurs as resets climb towards the $\dot{v} = 0$ nullcline before resetting again below threshold. This corresponds to chattering (Fig. 11 center, CH1 and right, CH2). Eqs. (32) and (38) provide estimates $\bar{\zeta}_2(T_{th})$ of $u(t^+_{peak})$, and refractory periods are approximated by the first two terms $T_{b1}(I') + T_{b2}(I')$ of Eq. (24). Interburst intervals and spike densities can be adjusted via c and d: increasing c produces longer interburst intervals and shorter ISIs (cf. Eq. (15)), and decreasing d can lengthen bursts and eventually cause a transition to above-threshold periodic spiking: see §3.3.1 and Fig. 8.

The examples in this section show that the approximations of instantaneous and asymptotic firing rates developed in §§3.2-3.3 are remarkably accurate, and offer explicit guidelines for fitting the RQIF model to particular neural responses, by predicting parameters I, a, b, c and d that yield desired transient and asymptotic behaviors.

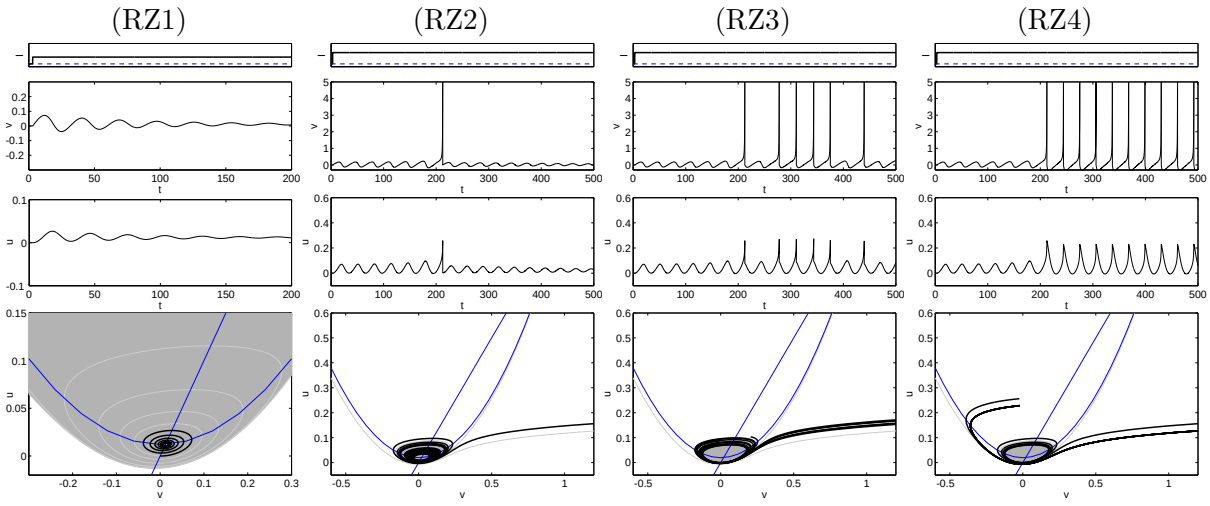

Figure 12: Typical RZ responses showing input current, voltage and recovery variable time series (top, second and third rows), and phase planes after application of I_{in} (bottom). RZ1: $I_{in} = 0.012,\ d = 0$: damped oscillations. RZ2: $I_{in} = 0.01986,\ d = -0.256$: single spike preceded bu growing oscillations and followed by damped oscillations. RZ3: $I_{in} = 0.01986,\ d = -0.18$: disordered train of oscillations and spikes. RZ4: $I_{in} = 0.01986,\ d = 0$: oscillations followed by slow periodic spiking. Parameters $a = 0.05,\ b = 1,\ c = 0$ throughout. Gray shading denotes $W^s(v_{rest})$, as in Fig. 4.

4.2 Case (b): $I < I_{SN}$

In the previous section input currents I_{in} were set large enough that no fixed points exist for $t > t^*$, and persistent spiking always occurs. For smaller $I_{in} < I_{SN} = b^2/4$ the fixed points survive, allowing richer dynamics related to the bifurcation sequences of §§3.1-5. In Fig. 12 we show typical examples as I_{in} is gradually increased. In the simplest case $I_{in} \ll I_{hom}$, v_{rest} is a sink with a large domain of attraction bounded below by $W^s(v_{th})$ (cf. Fig. 4(f)). When $(u, v) = (0, 0)$ lies in this domain and v_{rest} is a stable focus, such orbits exhibit damped oscillations (Fig. 12, RZ1), corresponding to resonator responses (Izhikevich, 2003, 2006).

Responses involving mixtures of oscillations and spikes can be obtained by increasing I_{in} past the homoclinic bifurcation into the range $I_{hom} < I_{in} < I_{AH}$, producing an unstable limit cycle that bounds $W^s(v_{rest})$ (cf. Figs. 4(c,b)). Behavior is governed by the position of the reset point determined by c and d. In the remaining panels of Fig. 12 we fix I_{in} along with a, b and c and increase d through -0.256 (RZ2), -0.18 (RZ3) to 0 (RZ4), so that all three cases have identical phase planes and differ only in reset points. In RZ2 the initial condition $(u, v) = (0, 0)$ lies near the limit cycle but outside of it, so that oscillations grow until a spike occurs, followed by reset within the limit cycle and damped oscillations. In both RZ3 and RZ4 resets following the first spike occur outside the limit cycle. This produces irregular spiking in RZ3, due to sensitive dependence as reset points cross the lower branch of $W^s(v_{th})$, while for larger d in RZ4 reset occurs above $W^u(v_{th})$, yielding slow periodic spiking typical of the below-threshold regime of §3.2.1.

We end this section by discussing responses to hyperpolarization and brief stimuli.

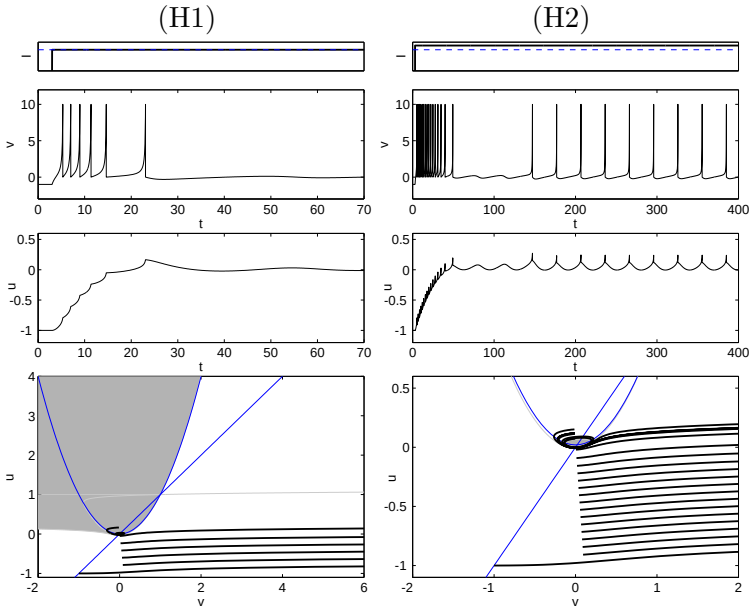

Figure 13: Responses to hyperpolarized input; same format as Fig. 12. H1: $I_{in}^a = -1.75,\ I_{in}^b = 0,\ d = 0$: hyperpolarized TC response, initial burst terminated by damped oscillations. H2: $I_{in}^a = -1.75,\ I_{in}^b = 0.01986,\ d = -0.12$: response combines fast spiking, subthreshold oscillations and slow periodic spiking. Parameters $a = 0.05,\ b = 1,\ c = 0$ throughout. Gray shading denotes $W^s(v_{rest})$, as in Fig. 4.

Post hyperpolarization rebound: Here the cell is subjected to a negative input current $I_{in}^a \ll I_{SN}$ for sufficiently long that its state converges to $(v(t^*), u(t^*))$, near v_{rest}, at which time the current jumps to $I_{in}^b \in [0, I_{SN}]$:

$$I_{hyp}(t) = \begin{cases} I_{in}^a < 0, & \text{if } t < t^*, \\ I_{in}^b \geq 0, & \text{if } t > t^*. \end{cases} \tag{40}$$

In this case, at $t = t^*$ the fixed points "jump" to new positions, and in particular for $I_{in}^b = 0$, v_{rest} jumps to $(v, u) = (0, 0)$. The system state is therefore initialized in the above-threshold regime and, for $d \geq 0$, emits a burst of spikes with increasing ISIs until it reaches the near- or below-threshold regime and is reset above the $\dot{v} = 0$ nullcline. If $I_{in}^b < I_{hom}$ and $W^s(v_{rest})$ is sufficiently large, reset occurs within that domain and the orbit converges to v_{rest}: Fig. 13(H1). This pattern is typical of thalamo-cortical neurons (TC). Increasing I_{in}^b above I_{hom} produces more complex behaviors similar to those of Fig. 12, so that the initial burst may be followed by oscillations and/or spikes. An example appears in Fig. 13(H2).

Responses to brief Stimuli: We now return to the injection of positive direct currents that create fixed points, but additionally insert one or more brief stimuli or impulses, represented as

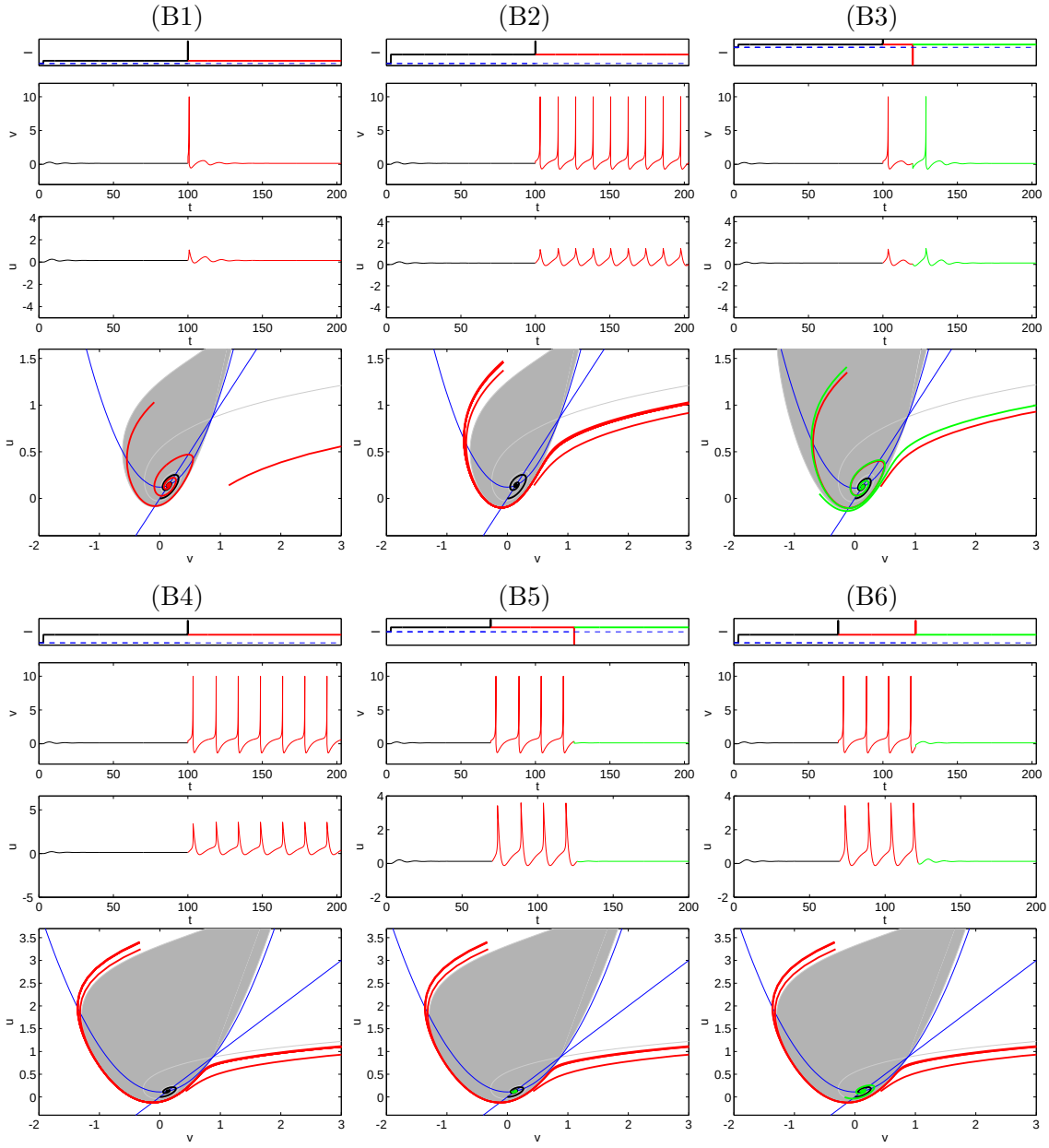

Figure 14: Responses to brief stimuli for $I_{in} < I_{hom}$; same format as Figs. 12-13. B1: $I_{in} = 0.12,\ s_{in} = 1,\ d = 0$: a large stimulus produces a single spike. B2: $I_{in} = 0.12,\ s_{in} = 0.3,\ d = 0$: a smaller stimulus produces slow periodic spiking. B3: $I_{in} = 0.11,\ s_{in}^{+} = 0.3,\ s_{in}^{-} = -0.65,\ d = 0$: positive and negative stimuli each produce one spike. B4: $I_{in} = 0.11,\ s_{in} = 0.3,\ d = 2$: slow periodic spiking with $d > 0$. B5: $I_{in} = 0.11,\ s_{in}^{+} = 0.3,\ s_{in}^{-} = -0.3,\ d = 2$: slow periodic spiking initiated by positive impulse and inhibited by negative impulse. BS6: $I_{in} = 0.11,\ s_{in}^{+} = 0.3,\ s_{in}^{+} = 0.3,\ d = 2$: Slow periodic spiking initiated and inhibited by a positive impulse. Parameters $a = 0.5,\ b = 1,\ c = 0$ throughout; note that $a,\ b$ are as in Fig. 4. Gray shading denotes $W^s(v_{rest})$, as in Fig. 4.

delta functions. In the case of a single impulse, the input current is

$$I_{bs}(t) = \begin{cases} 0, & \text{if } t < t^*, \\ I_{in} + s_{in}\delta(t - (t^* + t^s)), & \text{if } t > t^*. \end{cases} \tag{41}$$

Combinations of impulses and appropriate tuning of reset parameters can produce a considerable variety of responses, especially when the background input $I_{in} \lesssim I_{hom}$. In Fig. 14 we set $I_{in} = 0.12$ (B1, B2) and 0.11 (B3 - B6), $d = 0$ (B1 - B3) and $d = 2$ (B4 - B5), and apply positive and negative impulses of varying magnitudes s_{in}. As in §4.1, we analyse responses by considering the phase plane for $I = I_{in}$ with initial conditions at the origin. The delta function shifts the voltage from $v(t^s)$ to $v(t^s) + s_{in}$, so that the solution is reset at t^s as well as at t_{peak}, after each spike.

For $I_{in} \lesssim I_{hom}$, $W^s(v_{th})$ bounds a narrow trapping region $W^s(v_{rest})$ for the sink, as in Fig. 4(d). Solutions reset above this region exhibit slow periodic spiking, those reset within it are attracted to v_{rest}. Sufficiently large impulses can cause jumps in v that take orbits across $W^s(v_{th})$ in either direction. In Figs. 14(B1,B2) orbits escape from the trapping region due to positive (excitatory) impulses, but the large impulse (B1) places v with less time to grow to v_{peak}, so that $u(t^+_{peak}) + d$ is lower than for the small impulse (B2). Thus, after reset in B1 the orbit lies within $W^s(v_{rest})$, while in B2 it lies above it, with the counterintuitive effect that a small impulse can create repeated spiking (B2), while a large one might evoke only a single spike (B1).

As I_{in} decreases $W^s(v_{rest})$ grows, but if both branches of $W^s(v_{th})$ still limit on the right branch of the $\dot{v} = 0$ nullcline, as in Fig. 4(e), either positive or negative jumps in v can shift the orbit outside $W^s(v_{rest})$. Thus, for $d \approx 0$, impulses of either sign typically elicit single spikes: Fig. 14(B3), while for larger $d > 0$ post spike resets lie above $W^s(v_{th})$, resulting in periodic spiking (B4).

Both the timing and amplitudes of impulses influence responses. Solutions that have settled into periodic spiking circulate from reset in the near- or below-threshold region to the left of $W^s(v_{th})$ (see Fig. 4(e) and §3.2.1). When an impulse arrives, the position of $(v(t^s), u(t^s))$ relative to this manifold is clearly critical. If $v(t^s) > v_{rest}$, then positive impulses have little effect (merely advancing the next spike), and a negative impulse is required to place the orbit in $W^s(v_{rest})$ and terminate spiking (B5). In contrast, if $v(t^s) < v_{rest}$, a positive impulse is required to terminate spiking (B6), and negative impulses merely delay the next spike. These examples also show that different inputs and parameter sets can produce similar spike patterns (B2, B4 and B5, B6).

To further illustrate the importance of timing, in Fig. 15 we show the effects of three realizations of a train of ten impulses with prespecified amplitudes drawn from a uniform distribution $U(-1, 1)$, injected at times produced by a Poisson process with rate $\lambda = 0.025$. The resulting responses contain single spikes and bursts of differing lengths separated by damped oscillations, and one can also identify spikes that are delayed or advanced by the impulses. In BR1 and BR2, $I_{in} \lesssim I_{hom}$, so that the sensitive reset phenomena of Fig. 14 are in play. In BR3 a slight decrease in I_{in} has moved the left hand branch of $W^s(v_{th})$ below the $\dot{v} = 0$ nullcline, as in Fig 4(f), so that each impulse elicits at most a single spike (the second, third, fifth, sixth and eighth impulses are so small, or arrive at such times, that the orbit does not leave $W^s(v_{rest})$).

5 Conclusions

In this paper we review phase plane and bifurcation analyses of a quadratic integrate-and-fire neural model with a recovery variable (RQIF, Eq. (9)) (Izhikevich, 2003; Touboul, 2008; Touboul

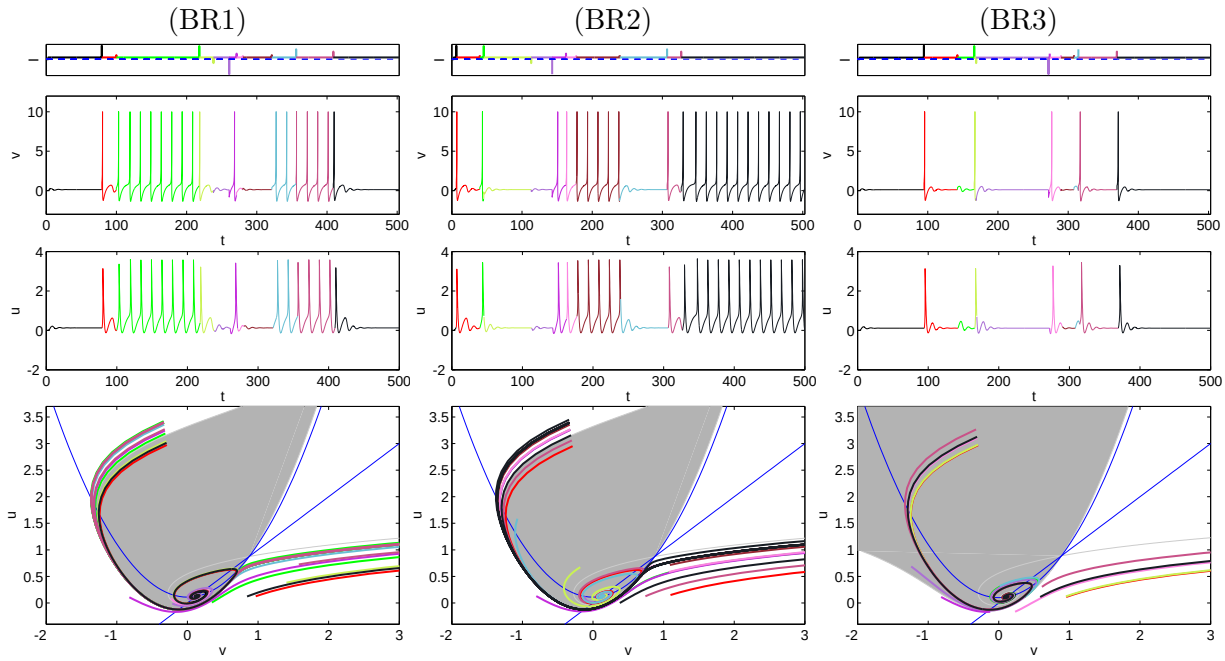

Figure 15: Effects of ten prespecified impulses s_{in} = 0.84, 0.25, 0.81, -0.24, -0.93, 0.35, 0.2, 0.25, 0.62, 0.47, drawn from a uniform distribution $U(-1, 1)$ and applied at random times; same format as Figs. 12-14. BR1 and BR2: $I_{in} = 0.11$: two realizations showing disordered spike trains. BR3: $I_{in} = 0.1$: for $I_{in} \ll I_{hom}$: each impulse causes at most a single spike. Parameters $a = 0.5$, $b = 1$, $c = 0$, $d = 2$ throughout; note that a, b are as in Fig. 4, and gray shading denotes $W^s(v_{rest})$.

and Brette, 2009). Local saddle-node and Andronov-Hopf bifurcations meet a branch of global homoclinic loop bifurcations at a codimension two Takens-Bogdanov point (Guckenheimer and Holmes, 1983; Kuznetsov, 2004), as illustrated in Fig. 3, with the corresponding phase portraits of Fig. 4. Our analysis differs from that of (Touboul, 2008; Touboul and Brette, 2009) in using a different normal form, "prepared" by means of a parameter-dependent translation (see Appendix: Eqs. (52-53)) that fixes the saddle point involved in the homoclinic loop at the origin. The blow-up transformation (57) is chosen to unfold the region near the codimension two bifurcation, where the adaptation parameter b and the time scale of the recovery variable a are comparable, and we checked that the predicted homoclinic bifurcation curve (13) is consistent with numerical computations. Moreover, with the saddle fixed, other limits such as $0 < a \ll b = \mathcal{O}(1)$ can be explored using appropriate blowup transformations. The computation provides a corrected estimate for the homoclinic bifurcation curve, which can be exploited in fitting the model to recordings of neural data.

In the case that the recovery variable evolves slowly relative to voltage ($a \ll 1$), we use phase plane dynamics to derive approximations of "instantaneous" firing rates in three adjacent input current ranges. We do this both for cases in which the system has no fixed points, so that periodic spiking always occurs (Fig. 6), and in which a hyperpolarized state exists, so that the system is bistable (Fig. 7). We find that firing rates decrease smoothly as input currents fall below threshold, unlike the one-dimensional LIF and QIF models which have zero firing rates in this range. As

the reset voltage c moves towards v_{peak}, the firing rate formulae reveal sharper transitions from high to low rates in the near-threshold regime, signalling the mechanism for bursting. For weaker separation of time scales ($a = \mathcal{O}(b)$), numerical computations show that instantaneous firing rates in the below-threshold range increase significantly with a (Fig. 6).

We then use the instantaneous firing rate estimates in deriving one-dimensional averaged systems that capture asymptotic behavior for $a \ll 1$ and $d = 0$. Proofs of existence, uniqueness and stability of fixed points in the averaged equations for both $c = 0$ and $c > 0$ allow us to compute parameter regimes for which the solutions asymptote to periodic dynamics, and hence to obtain asymptotic firing rate curves. For $d \neq 0$, we study the dynamics via an Euler map approximation of the averaged ODE. Solving for the fixed point of this map yields a family of firing rate curves (Fig. 8), and the combination of instantaneous and asymptotic firing rates provides a complete, analytical characterization of the dynamical regimes of the RQIF.

To illustrate the use of our analysis, we revisit and extend the work of (Izhikevich, 2003, 2006). We further provide examples of steady state and transient responses to impulses and constant current steps, characteristic of different classes of cortical neurons, and we explain how the interaction of phase plane dynamics and post-spike reset points produces specific spiking patterns. The choices of bifurcation and reset parameters used to generate Figs. 9-15 were guided by our phase plane and firing rate studies, and the presence or absence of fixed points is again a key determinant of behavior. In the former case, the domain of attraction of the stable hyperpolarized state is bounded by the stable manifold of the saddle point, and the location of this curve relative to the slow manifold largely controls whether orbits remain below threshold, or produce a spike after each reset. In the latter case asymptotic firing rates are used to place the RQIF in a desired regime, and by doing this we demonstrate the precision of the averaging approximation. The instantaneous firing rates help to elucidate the dynamics and transitions among different regimes (fourth row of Figs. 9-11).

We believe that these results will be useful in adapting RQIF models in large-scale brain simulations such as those of (Izhikevich and Edelman, 2008). In future work we propose to compute firing rate curves for an RQIF model with a recovery variable and additive Gaussian noise.

Appendix: Computational details for §§3.1 and 3.3.1

Saddle-node and Andronov-Hopf bifurcations

Linearizing the RQIF model (9) at the fixed points results in the Jacobian matrix

$$Df\Big|_{(u,v)=(u_f^\pm, v_f^\pm)} = \begin{bmatrix} 2v_f^\pm & -1 \\ ab & -a \end{bmatrix}, \tag{42}$$

with eigenvalues and eigenvectors:

$$\lambda_{1,2} = -\frac{a}{2} + v_f^\pm \pm \frac{1}{2}\sqrt{4(v_f^\pm)^2 + a^2 - 4a(b - v_f^\pm)}, \tag{43}$$

$$v_{1,2} = \left(1, 2v_f^\pm - \lambda_{1,2}\right)^T. \tag{44}$$

Elementary calculations and appeal to the bifurcation results in (Guckenheimer and Holmes, 1983, §3.4) then yield the SN and AH bifurcation curves of Eqs. (11-12).

To compute the first Lyapunov (stability) coefficient for the AH bifurcation we set $b = ka > a$ (choosing $k > 1$), so that the bifurcation occurs at $I_{AH} = a^2(2k-1)/4$ (cf. Eq. (12)), and the fixed

point lies at $(v_{rest}, u_{rest}) = (a/2, ka^2/2)$. To bring the system to normal form we first translate the fixed point to the origin by setting $v = a/2 + \bar{v}$ and $u = ka^2/2 + \bar{u}$, obtaining $\dot{w} = Lw + N(w)$:

$$\begin{bmatrix} \dot{\bar{v}} \\ \dot{\bar{u}} \end{bmatrix} = \begin{bmatrix} a & -1 \\ ka^2 & -a \end{bmatrix} \begin{bmatrix} \bar{v} \\ \bar{u} \end{bmatrix} + \begin{bmatrix} \bar{v}^2 \\ 0 \end{bmatrix}. \tag{45}$$

A similarity transformation $y = T^{-1}w$ then takes L into normal form:

$$\begin{bmatrix} \dot{y_1} \\ \dot{y_2} \end{bmatrix} = \begin{bmatrix} 0 & -a\sqrt{k-1} \\ a\sqrt{k-1} & 0 \end{bmatrix} \begin{bmatrix} y_1 \\ y_2 \end{bmatrix} + \begin{bmatrix} y_2^2/\sqrt{k-1} \\ y_2^2 \end{bmatrix}, \tag{46}$$

where the columns of T are the imaginary and real parts of the eigenvectors of L. Letting $f = y_2^2/\sqrt{k-1}$, $g = y_2^2$ and subindices denote partial derivatives with respect to y_1 and y_2, we use the formula developed in (Guckenheimer and Holmes, 1983, §3.4, Eq. (3.4.11)) to calculate the first Lyapunov coefficient:

$$c_3 = \frac{1}{16}(f_{111} + f_{122} + g_{221} + g_{222}) + \frac{1}{16a\sqrt{k-1}}(f_{12}(f_{12} + f_{22}) - g_{12}(g_{11} + g_{22}) - f_{11}g_{11} + f_{22}g_{22}). \tag{47}$$

For Eq. (46) the only nonzero terms are $f_{22} = 2/\sqrt{k-1}$ and $g_{22} = 2$ and hence

$$c_3 = \frac{1}{4a(k-1)} > 0, \tag{48}$$

implying that the AH bifurcation is subcritical and the limit cycle is unstable for all $b > a$.

Takens-Bogdanov normal form

Let $a > 0$ be fixed and b and I be variable parameters. When $I = a^2/4$ and $b = a$ the degenerate fixed point lies at $v_f = a/2, u_f = a^2/2$ and the Jacobian matrix (42) has a zero eigenvalue with algebraic multiplicity two and only one eigenvector. Universal unfoldings of planar systems with such linear parts were studied by Takens (Takens, 1974) and Bogdanov (Bogdanov, 1975), see (Guckenheimer and Holmes, 1983, §7.3). To derive the normal form we first translate the fixed point to the origin by letting $v = \bar{v} + a/2,\ u = \bar{u} + a^2/2$ and we replace I and b by

$$\tilde{I} = I - a^2/4 \ \text{ and } \ \tilde{b} = b - a, \tag{49}$$

so that the SN and AH bifurcation curves become $\tilde{I}_{SN} = a\tilde{b}/2 + \tilde{b}^2/4$ and $\tilde{I}_{AH} = a\tilde{b}/2$, and $\tilde{I} = \tilde{b} = 0$ at the codimension two bifurcation point[1]. The RQIF system in $\bar{v}$ and $\bar{u}$ variables can then be rewritten as $\dot{w} = Lw + N(w) + P(w; \tilde{I}, \tilde{b})$:

$$\begin{bmatrix} \dot{\bar{v}} \\ \dot{\bar{u}} \end{bmatrix} = \begin{bmatrix} a & -1 \\ a^2 & -a \end{bmatrix} \begin{bmatrix} \bar{v} \\ \bar{u} \end{bmatrix} + \begin{bmatrix} \bar{v}^2 \\ 0 \end{bmatrix} + \begin{bmatrix} \tilde{I} \\ a(\tilde{b}\bar{v} + \frac{a\tilde{b}}{2}) \end{bmatrix}, \tag{50}$$

where $w = (\bar{v}, \bar{u})^T$, L is the linear term, $N(w)$ includes the nonlinear terms independent of parameters and $P(w; \tilde{I}, \tilde{b})$ includes the parameter-dependent terms, which are linear in $\bar{v}$. A similarity

[1]The parameters $\tilde{I}, \tilde{b}$ correspond to I_1 and b_1 in (Touboul, 2008; Touboul and Brette, 2009).

transformation T whose columns are the eigenvector $(1,\ a)^T$ and generalized eigenvector $(1,\ a-1)^T$ of L brings the linear part into Jordan form:

$$\begin{bmatrix}\dot{y}_1\\ \dot{y}_2\end{bmatrix} = \begin{bmatrix}0 & 1\\ 0 & 0\end{bmatrix}\begin{bmatrix}y_1\\ y_2\end{bmatrix} + \begin{bmatrix}(1-a)(y_1+y_2)^2\\ a(y_1+y_2)^2\end{bmatrix} + \begin{bmatrix}(1-a)\tilde{I}+a\tilde{b}(y_1+y_2+\frac{a}{2})\\ a\tilde{I}-a\tilde{b}(y_1+y_2+\frac{a}{2})\end{bmatrix}, \tag{51}$$

where $y = T^{-1}w$ and $T^{-1}LT = J = \begin{bmatrix}0 & 1\\ 0 & 0\end{bmatrix}$.

Before computing the normal form, we apply a further, parameter-dependent translation that fixes the saddle point v_{th} at the origin, the reason for which is explained at the end of this appendix. The saddle point of Eq. (51) is located at (y_1^s, y_2^s), where

$$y_1^s + y_2^s = \frac{\tilde{b}+\sqrt{K}}{2},\quad y_2^s = -\frac{\tilde{b}}{2}\left(\tilde{b}+a+\sqrt{K}\right),\quad \text{with}\quad K = \tilde{b}^2 - 4(\tilde{I}-a\tilde{b}/2). \tag{52}$$

Letting $y_1 = \bar{y}_1 + y_1^s,\ y_2 = \bar{y}_2 + y_2^s$ and dropping the bars, Eq. (51) becomes

$$\begin{bmatrix}\dot{y}_1\\ \dot{y}_2\end{bmatrix} = \begin{bmatrix}0 & 1\\ 0 & 0\end{bmatrix}\begin{bmatrix}y_1\\ y_2\end{bmatrix} + \begin{bmatrix}(1-a)(y_1+y_2)^2\\ a(y_1+y_2)^2\end{bmatrix} + \begin{bmatrix}(\tilde{b}+(1-a)\sqrt{K})(y_1+y_2)\\ a\sqrt{K}(y_1+y_2)\end{bmatrix}. \tag{53}$$

In the Bogdanov normal form a further quadratic transformation eliminates scalar multiples of the four vectorfields

$$\begin{bmatrix}y_2^2\\ 0\end{bmatrix}, \begin{bmatrix}0\\ y_2^2\end{bmatrix}, \begin{bmatrix}y_1y_2\\ 0\end{bmatrix}\quad\text{and}\quad\begin{bmatrix}y_1^2\\ -2y_1y_2\end{bmatrix} \tag{54}$$

(Guckenheimer and Holmes, 1983, §3.3), so that the first component of the nonlinear term in (53) can be nullified and the second retains only y_1^2 and y_1y_2 terms:

$$\begin{bmatrix}\dot{y}_1\\ \dot{y}_2\end{bmatrix} = \begin{bmatrix}0 & 1\\ 0 & 0\end{bmatrix}\begin{bmatrix}y_1\\ y_2\end{bmatrix} + \begin{bmatrix}0\\ ay_1^2+2y_1y_2\end{bmatrix} + \begin{bmatrix}(\tilde{b}+(1-a)\sqrt{K})(y_1+y_2)\\ a\sqrt{K}(y_1+y_2)\end{bmatrix} + \mathcal{O}(|y_j|^3). \tag{55}$$

Blowing up, Melnikov's method and homoclinic bifurcation

To prove that a homoclinic bifurcation occurs, we must show that a homoclinic orbit for a "blown-up" degenerate system at $\tilde{I} = \tilde{b} = 0$ persists as one leaves this point on a specific path in the parameter space. From the analysis of the simpler unfoldings in (Guckenheimer and Holmes, 1983, §7.3) and (Kuznetsov, 2004, §8.4), we expect this to occur on a curve $\tilde{I} = \tilde{I}_{hom} = a\tilde{b}/2 + \mathcal{O}(\tilde{b}^2)$. It is convenient to introduce a further translation $\tilde{I} = \bar{I} + a\tilde{b}/2$, so that the parameter K (Eq. (52)) and expected homoclinic bifurcation curve become

$$K = \tilde{b}^2 - 4\bar{I}\,,\ \bar{I}_{hom} = \nu\tilde{b}^2 + \mathcal{O}(\tilde{b}^3), \tag{56}$$

where ν is the coefficient of $\tilde{b}^2$ that we seek. We can then adopt the same blow-up scaling of state variables, parameters, and time as used in (Guckenheimer and Holmes, 1983, §7.3):

$$y_1 = \varepsilon^2 x_1, y_2 = \varepsilon^3 x_2, \tilde{b} = \varepsilon^2, \bar{I} = \varepsilon^4\nu, t \mapsto \varepsilon t, \tag{57}$$

under which d/dt becomes $\varepsilon d/dt$, $\sqrt{K} = \varepsilon^2\sqrt{1-4\nu}$, and Eq. (55) becomes

$$\begin{aligned}
\dot{x}_1 &= x_2 + \varepsilon[(1+(1-a)\eta]x_1 + \mathcal{O}(\varepsilon^2),\\
\dot{x}_2 &= (\eta + x_1)x_1 + \varepsilon(a\eta + 2x_1)x_2 + \mathcal{O}(\varepsilon^2),\\
&\text{where } \ \eta = \sqrt{1-4\nu}.
\end{aligned} \tag{58}$$

For $\varepsilon = 0$, Eq. (58) is Hamiltonian with

$$H_0 = -\frac{x_2^2}{2} + a(\frac{\eta x_1^2}{2} + \frac{x_1^3}{3}) \tag{59}$$

and has a homoclinic orbit that can be written explicitly as

$$x_1^0(t) = -3/2\eta\left(\mathrm{sech}^2\left(\frac{\sqrt{a\eta}t}{2}\right)\right) \stackrel{\text{def}}{=} -3/2\eta S^2, \tag{60}$$

$$x_2^0(t) = 3/2\sqrt{a}\eta^{3/2}\tanh\left(\frac{\sqrt{a\eta}t}{2}\right)\mathrm{sech}^2\left(\frac{\sqrt{a\eta}t}{2}\right) \stackrel{\text{def}}{=} 3/2\sqrt{a}\eta^{3/2}TS^2. \tag{61}$$

To determine the fate of this homoclinic orbit for $\varepsilon > 0$ it suffices to compute the first order Melnikov function M_1 as described in (Melnikov, 1963) and (Guckenheimer and Holmes, 1983, §4.5). Writing Eq. (58) in the form

$$\dot{x} = f(x) + \varepsilon g(x) + \mathcal{O}(\varepsilon^2), \tag{62}$$

M_1 is given by the following integral around the unperturbed orbit:

$$M_1 = \int_{-\infty}^{+\infty} f(x^0(t)) \wedge g(x^0(t))dt,$$

and the distance between the perturbed unstable and stable manifolds to the saddle at the point $x^0(0)$ is given by

$$x^u(0) - x^s(0) = \frac{\varepsilon M_1}{|f(x^0(0))|} + \mathcal{O}(\varepsilon^2). \tag{63}$$

Using Eqs. (60-61), computation of M_1 is straightforward:

$$M_1 = \int_{-\infty}^{+\infty} x_2^0(t)^2\left[2x_1^0(t) + a\eta\right] - ax_1^0(t)^2(\eta + x_1^0(t))\left[1 + (1-a)\eta\right]dt = -\frac{6}{35}\sqrt{a}\eta^{5/2}(5\eta - 7). \tag{64}$$

Eqs. (63) and (64) imply that $x^u(0) - x^s(0) = 0$ and the homoclinic loop is preserved on a parameter set satisfying

$$5\eta - 7 = \mathcal{O}(\varepsilon) \ \Rightarrow \ \nu = -\frac{6}{25} + \mathcal{O}(\varepsilon). \tag{65}$$

Letting $\varepsilon \to 0$ and transforming back from $\bar{I}$ to $\tilde{I}$, we deduce that the homoclinic bifurcation curve emerges from the codimension two point $\tilde{I} = \tilde{b} = 0$ as

$$\tilde{I} = \tilde{I}_{hom} = \frac{a\tilde{b}}{2} + \nu\tilde{b}^2 + \mathcal{O}(\tilde{b}^3). \tag{66}$$

Finally, transforming to the original parameters I and b and inserting the value of ν yields Eq. (13).

We close by explaining why the transformation that fixes v_{th} at $(0,0)$ was introduced (see Eqs. (52-53) above). Direct application of the normal form transformation and blow-up scaling of (57) to Eq. (51) produces a singular $\mathcal{O}(\varepsilon^{-1})$ term that drives the saddle to infinity as $\varepsilon \to 0$, invalidating the Melnikov perturbation calculations above. Although a different scaling removes this problem, it leaves the $\mathcal{O}(\varepsilon)$ system analogous to (58) degenerate, necessitating a laborious second order Melnikov calculation (Liu, 1990), for which the resulting prediction of the homoclinic bifurcation curve is insufficiently accurate for reasonable values of $\tilde{I}$, $\tilde{b}$.

Proof that Eqs. (30) and (36) have unique stable fixed points

Although Eq. (30) is a special case of (36), the proof for the former is simpler and prepares the way for the general case, so we treat it first. For fixed $c = 0$ and I, b and $v_{peak} > 0$, the function $\bar{h}_2(\bar{\zeta}_2)$ limits on $bv_{peak}/2$ and 0 as $\bar{\zeta}_2 \to -\infty$ and $\bar{\zeta}_2 \to I$. We claim that the derivative $\bar{h}_2'(\bar{\zeta}_2) < 0$ on $(-\infty, I)$, which implies that there is a unique solution $\bar{\zeta}_2^{fp} \in (0, I)$ to the equation $\bar{h}_2(\bar{\zeta}_2) - \bar{\zeta}_2 = 0$. Moreover, this is a stable, hyperbolic fixed point, since $\bar{h}_2'(\bar{\zeta}_2^{fp}) - 1 < 0$.

To prove the claim we compute

$$\bar{h}_2'(\bar{\zeta}_2) = \frac{-b\eta}{4v_{peak}(1+\eta^2)\,\mathrm{atan}(\eta)} \left[\left(1 + \eta^2 + \frac{\eta}{\mathrm{atan}(\eta)} \right) \ln\left(1+\eta^2\right) - 2\eta^2 \right], \tag{67}$$

where $\eta = v_{peak}/\sqrt{I - \bar{\zeta}_2} \in (0, \infty)$. The prefactor $-b\eta/\ldots$ is strictly negative. We will show that the quantity in square brackets is strictly positive for $\eta \in (0,\infty)$ ($I \in (-\infty, 0)$). Since $\eta/\mathrm{atan}(\eta) \geq 1$, it suffices to show that

$$\ln(1+\eta^2) \geq \frac{2\eta^2}{(2+\eta^2)}. \tag{68}$$

At $\eta = 0$ both left and right hand sides of inequality (68) are zero, so if we can show that the values of their derivatives are ordered in the same sense, i.e., that

$$\frac{2\eta}{1+\eta^2} > \frac{8\eta}{(2+\eta^2)^2} \quad \text{for} \quad \eta > 0, \tag{69}$$

then our claim is true. But simplification shows that inequality (69) is equivalent to the claim that $\eta^4 > 0$, which clearly holds for all $\eta > 0$. This concludes the proof for Eq. (30), the case $c = 0$.

For $c > 0$, it is convenient to define the ratio $\kappa = c/v_{peak}$. We note that $\kappa \in (0,1)$, because $0 < c < v_{peak}$, and that $\bar{h}_2(\bar{\zeta}_2)_{c>0}$ limits on the values $bv_{peak}(1+\kappa)/2$ and 0 as $\bar{\zeta}_2 \to -\infty$ and $\bar{\zeta}_2 \to I + c^2$. Since $bv_{peak}(1+\kappa)/2 > 0$, to establish existence, uniqueness and stability of the fixed point, it again suffices to prove that the derivative $\bar{h}_2'(\bar{\zeta}_2)_{c>0} < 0$. Differentiating the two expressions of Eq. (36), we obtain

$$\begin{aligned}
&\bar{h}_2'(\bar{\zeta}_2)_{c>0} = \frac{-b\,\eta}{4v_{peak}(1+\eta^2)(1+\kappa^2\eta^2)\,\mathrm{atan}(T_1(\eta))} \times \\
&\left[\left((1+\eta^2)(1+\kappa^2\eta^2) + (1-\kappa\eta^2)\frac{(1-\kappa)\eta}{\mathrm{atan}(T_1(\eta))} \right) \ln(L_1(\eta)) - 2\,(1-\kappa^2)\,\eta^2 \right] \quad \text{for} \quad \bar{\zeta}_2 < I \qquad (70) \\
&= \frac{-b\,\rho}{4v_{peak}(\rho^2-1)(\kappa^2\rho^2-1)\,\mathrm{atanh}(T_2(\rho))} \times \\
&\left[\left((\kappa\rho^2+1)\frac{(1-\kappa)\rho}{\mathrm{atanh}(T_2(\rho))} - (\rho^2-1)(\kappa^2\rho^2-1) \right) \ln(L_2(\rho)) - 2\,(1-\kappa^2)\,\rho^2 \right] \quad \text{for} \quad \bar{\zeta}_2 > I, \qquad (71)
\end{aligned}$$

where $\eta = v_{peak}/\sqrt{I-\bar{\zeta}_2} \in (0,\infty)$ as above, $\rho = v_{peak}/\sqrt{\bar{\zeta}_2 - I} \in (1/\kappa,\infty)$, and

$$T_1(\eta) = \frac{(1-\kappa)\,\eta}{1+\kappa\eta^2} \geq 0,\ L_1(\eta) = \frac{1+\eta^2}{1+\kappa^2\eta^2} \geq 1,\ T_2(\rho) = \frac{(1-\kappa)\,\rho}{\kappa\rho^2-1} \geq 0,\ L_2(\rho) = \frac{\rho^2-1}{\kappa^2\rho^2-1} \geq 1. \tag{72}$$

As in Eq. (67), the prefactors of Eqs. (70-71) are both strictly negative, so it again suffices to prove that the quantities in square brackets are strictly positive. For Eq. (70) this is complicated by the change in sign of $(1-\kappa\eta^2)$. For $\eta \in (0, 1/\sqrt{\kappa}]$ it is nonnegative, as are both expressions multiplying the logarithm, and we may generalize the lower bound $\eta/\mathrm{atan}(\eta) \geq 1$, using the fact that

$$\mathrm{atan}(T_1(\eta)) \leq T_1(\eta) \ \Rightarrow\ (1+\kappa\eta^2) \leq \frac{(1-\kappa)\eta}{\mathrm{atan}(T_1(\eta))}. \tag{73}$$

Thus, the expression multiplying the logarithm in Eq. (70) can be bounded below by

$$(1+\eta^2)(1+\kappa^2\eta^2) + (1-\kappa\eta^2)(1+\kappa\eta^2) = 2 + (1+\kappa^2)\eta^2, \tag{74}$$

and it suffices to show that

$$\ln(L_1(\eta)) = \ln\left(\frac{1+\eta^2}{1+\kappa^2\eta^2}\right) > \frac{2(1-\kappa^2)\eta^2}{2+(1+\kappa^2)\eta^2} \quad \text{for} \quad \eta > 0. \tag{75}$$

At $\eta = 0$ both left and right hand sides of inequality (75) are zero and, computing their derivatives as for the case $c = 0$ we obtain the following sufficient condition:

$$\frac{2\left(1-\kappa^2\right)\eta}{\left(1+\eta^2\right)\left(1+\kappa^2\eta^2\right)} > \frac{8\left(1-\kappa^2\right)\eta}{\left(2+\left(1+\kappa^2\right)\eta^2\right)^2} \quad \Longleftrightarrow \quad (1-\kappa^2)^2\eta^4 > 0. \tag{76}$$

which clearly holds for all $\eta > 0$ and $\kappa \in [0,1)$.

When $(1-\kappa\eta^2) < 0$ we may bound $1/\mathrm{atan}(T_1(\eta))$ from above using

$$\frac{1}{\mathrm{atan}(T_1(\eta))} \leq \frac{\sqrt{1+T_1(\eta)^2}}{T_1(\eta)} \ \Rightarrow\ \frac{(1-\kappa)\eta}{\mathrm{atan}(T_1(\eta))} \leq \sqrt{(1+\eta^2)(1+\kappa^2\eta^2)} \stackrel{\mathrm{def}}{=} A_1. \tag{77}$$

Employing this bound in the same manner as above we obtain the sufficient condition

$$\ln(L_1(\eta)) > \frac{2\left(1-\kappa^2\right)\eta^2}{X_1}, \quad \text{where} \quad X_1 = A_1(A_1 - (\kappa\eta^2 - 1)). \tag{78}$$

We can verify that inequality (78) holds at $\eta = 1/\sqrt{\kappa}$ and again take derivatives of its right and left hand sides to show that they are appropriately ordered. Using the identity $(2X_1 - \eta X_1')/X_1^2 = (\kappa\eta^2+1)/A_1^3$ (discovered using Mathematica and verified analytically), we finally obtain the following sufficient condition

$$\frac{2\left(1-\kappa^2\right)\eta}{A_1^2} > \frac{2\left(1-\kappa^2\right)\left(1+\kappa\eta^2\right)\eta}{A_1^3} \quad \Longleftrightarrow \quad A_1^2 > 1+\kappa\eta^2 \quad \Longleftrightarrow \quad (1-\kappa)^2\eta^2 > 0,$$

which clearly holds for all $\eta > 0$ and $\kappa \in [0,1)$. Further details of the derivation are available from the first author.

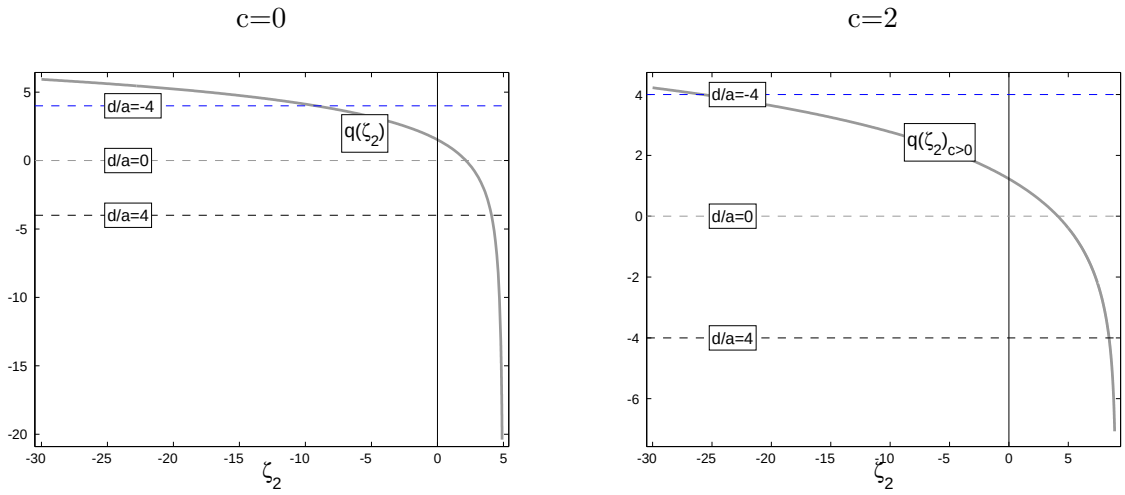

Figure 16: Fixed points of the single-step Euler map for the averaged equation with $I = 5$, $b = 1$, $v_{peak} = 10$ and $a = 0.05$. Gray curves show $q(\bar{\zeta}_2)$ for $c = 0$ (left) and $q(\bar{\zeta}_2)_{c>0}$ for $c = 2$ (right), and their intersections with each dashed line, $-d/a$, for $d = -0.2$ (blue), $d = 0$ (gray) and $d = 0.2$ (black) denote the unique fixed point for the corresponding value of d.

We now turn to Eq. (71). It can be verified that the required inequality holds as $\rho \to 1/\kappa$ and $\rho \to \infty$. Since the first term multiplying the logarithm is positive definite and the second is negative definite, we require a lower bound on the first. The analogue to (77) is

$$\frac{1}{\operatorname{atanh}(T_2(\rho))} \geq \frac{\sqrt{1-T_2(\rho)^2}}{T_2(\rho)} \;\Rightarrow\; \frac{(1-\kappa)\rho}{\operatorname{atanh}(T_2(\rho))} \geq \sqrt{(\rho^2-1)(\kappa^2\rho^2-1)} \stackrel{\text{def}}{=} A_2, \tag{79}$$

and use of this in Eq. (71) results in the following inequality

$$\ln(L_2(\rho)) > \frac{2\,(1-\kappa^2)\,\rho^2}{X_2}, \quad \text{where} \quad X_2 = A_2(\kappa\rho^2 + 1 - A_2). \tag{80}$$

Using the identity $(2X_2 - \rho X_2')/X_2^2 = (1-\kappa\rho^2)/A_2^3$ (analogous to that used in the case above), we find that the derivative of the left hand side of (80) is larger than that of its right hand side, so that we expect inequality (80) to hold from the point at which its left hand side is greater or equal to its right hand side. Unfortunately, this does not occur at the endpoint $\rho = 1/\kappa$: at this point $X_2 = 0$ and $\ln(L_2(\eta)) = 2$, so the left hand side, multiplied by X_2, vanishes while the right hand side is positive for $\kappa \in (0,1)$. We find numerically that for $\rho \geq \rho_c = 2/\kappa$ the inequality holds for all $\kappa \in (0,1)$. Thus, in conjunction with the derivative argument, we conclude that for all $\rho > \rho_c = 2/\kappa$ the inequality holds. For $\rho < (1/\kappa, 2/\kappa)$ we can verify numerically that the inequality of Eq. (71) holds. This concludes the (computer-assisted) proof for the case $c > 0$. Also see the $d = 0$ cases of Fig. 16 for numerical evidence of unique fixed points.

The single-step Euler maps (32) **and** (37) **and their fixed points**

The fixed point $\bar{\zeta}_2^{fp}$ of the map (32) for $c = 0$ is determined by:

$$q(\bar{\zeta}_2^{fp}) = \left(h_2(\bar{\zeta}_2^{fp}) - \bar{\zeta}_2^{fp}\right) T_a(I - \bar{\zeta}_2^{fp}) = \frac{-d}{a}, \quad \text{or} \tag{81}$$

$$h_2(\bar{\zeta}_2^{fp}) - \bar{\zeta}_2^{fp} = \frac{-d}{aT_a(I - \bar{\zeta}_2^{fp})}. \tag{82}$$

For $d = 0$ Eq. (82) is the fixed point equation of the averaged ODE (30), and the proof above implies that its left-hand side decreases monotonically from ∞ to $-I$ as $\bar{\zeta}_2$ goes from $-\infty$ to I, crossing zero in the interval $0 < \bar{\zeta}_2 < I$. Since T_a increases monotonically from 0 to ∞ over this domain, for $d > 0$ the right-hand side of Eq. (82) also increases monotonically from $-\infty$ to 0, guaranteeing the existence of a unique solution $\bar{\zeta}_2^{fp} \in (0, I)$. Perturbative arguments imply that a unique fixed point persists for $d < 0$ with $|d|$ small, but since the right-hand side of (82) is monotonically decreasing for $d < 0$, fixed points need no longer exist for larger $|d|$, and if they do, uniqueness can fail. In fact for sufficiently large negative $d < 0$ no fixed point exists. Replacing $h_2(\bar{\zeta}_2^{fp})$ with $h_2(\bar{\zeta}_2^{fp})_{c>0}$ in Eq. (82), similar monotonicity arguments can be applied to establish existence, uniqueness and stability of the fixed point for $c > 0$.

For small $aT_a(I-\bar{\zeta}_2^{fp})$ the fixed point is stable since the map is the forward Euler approximation to the ODE (30) which has a unique stable fixed point. To illustrate that unique fixed points apparently exist over a range including relatively large negative d, in Fig. 16 we plot the left- and right-hand sides of Eq. (81). Alas, a proof that the left-hand side of this equation decreases monotonically continues to elude us.

Acknowledgments This work was partially supported by the University of Washington Department of Applied Mathematics and the Air Force Research Laboratory under FA9550-07-1-0537.

References

Amit, D. and Tsodyks, M. (1991). Quantitative study of attractor neural network retrieving at low spike rates I: substrate-spikes, rates and neuronal gain. *Network*, 2:259–274.

Bogdanov, V. (1975). Versal deformations of a singular point on the plane in the case of zero eigenvalues. *Functional Analysis and its Applications*, 9(2):144–145.

Connor, J., Walter, D., and Mckown, R. (1977). Neural repetitive firing - modifications of Hodgkin-Huxley axon suggested by experimental results from crustacean axons. *Biophys. J.*, 18:81–102.

Connors, B. and Gutnick, M. (1990). Intrinsic firing patterns of diverse neocortical neurons. *Trends in Neurosciences*, 13(3):99–104.

Ermentrout, G. (1998). Linearization of F-I curves by adaptation. *Neural computation*, 10(7):1721–9.

Ermentrout, G. and Kopell, N. (1986). Parabolic bursting in an excitable system coupled with a slow oscillation. *SIAM J. on Appl. Math.*, 46(2):233–253.

Ermentrout, G. and Terman, D. (2010). *Mathematical Foundations of Neuroscience*. Springer-Verlag, New York.

FitzHugh, R. (1961). Impulses and physiological states in theoretical models of nerve membrane. *Biophys. J.*, 1(6):445–466.

Gray, C. and McCormick, D. (1996). Chattering cells: Superficial pyramidal neurons contributing to the generation of synchronous oscillations in the visual cortex. *Science*, 274(5284):109–113.

Guckenheimer, J. and Holmes, P. (1983). *Nonlinear Oscillations, Dynamical Systems, and Bifurcations of Vector Fields (Applied Mathematical Sciences Vol. 42)*. Springer.

Hodgkin, A. and Huxley, A. (1952). A quantitative description of membrane current and its application to conduction and excitation in nerve. *J. Physiol.*, 117:500–544.

Izhikevich, E. (2003). Simple model of spiking neurons. *IEEE Transactions on Neural Networks*, 14:1569–72.

Izhikevich, E. (2006). *Dynamical Systems in Neuroscience: The Geometry of Excitability and Bursting*. MIT Press.

Izhikevich, E. (2010). Hybrid spiking models. *Phil. Trans. Roy. Soc. Lond. A*, 368:5061–5070.

Izhikevich, E. and Edelman, G. (2008). Large-scale model of mammalian thalamocortical systems. *Proc. Natl. Acad. of Sciences*, 105:3593–3598.

Keener, J. and Sneyd, J. (1998). *Mathematical Physiology*. Springer Verlag, New York.

Knight, B. (1972). Dynamics of encoding in a population of neurons. *J. Gen. Physiol.*, 59:734–766.

Kuznetsov, Y. (2004). *Elements of Applied Bifurcation Theory (Applied Mathematical Sciences Vol. 112)*. Springer-Verlag. 3rd Edition.

Liu, Z. (1990). Second order Melnikov function and its application. *Phys. Lett. A*, 143(4-5):213–216.

McCormick, D., Connors, B., Lighthall, J., and Prince, D. (1985). Comparative electrophysiology of pyramidal and sparsely spiny stellate neurons of the neocortex. *J. Neurophysiol.*, 54(4):782–806.

Melnikov, V. (1963). On the stability of the center for time-periodic perturbations. *Trans. Moscow Math. Soc.*, 12:1–57.

Nagumo, J., Arimoto, S., and Yoshizawa, S. (1962). An active pulse transmission line simulating a nerve axon. *Proc. IRE*, 50:2061–2070.

Rinzel, J. (1985). Excitation dynamics: Insights from simplified membrane models. *Fed. Proc.*, 37:2944–2946.

Rinzel, J. and Ermentrout, G. B. (1989). Analysis of neural excitability and oscillations. In *Methods in Neuronal Modeling*, pages 135–169. MIT Press, Cambridge, MA, USA.

Sanders, J., Verhulst, F., and Murdock, J. (2007). *Averaging Methods in Nonlinear Dynamical Systems*. Springer. 2nd Edition.

Stein, R. (1965). A theoretical analysis of neuronal variability. *Biophys. J.*, 5:173–194.

Takens, F. (1974). Forced oscillations and bifurcations. In *Applications of Global Analysis 1*, pages 1–59. Commun. Math. Inst. Rijksuniversiteit Utrecht 3. Reprinted in *Global Analysis of Dynamical Systems*, H.W. Broer, B. Krauskopf and G. Vegter (eds), Institute of Physics Publishing, Bristol, UK, pp 1-61, 2001.

Touboul, J. (2008). Bifurcation analyis of a general class of nonlinear integrate-and-fire neurons. *SIAM J. on Appl. Math.*, 68:1045–1079.

Touboul, J. (2009). Importance of the cutoff value in the quadratic adaptive integrate-and-fire model. *Neural Computation*, 21:2114–2122.

Touboul, J. and Brette, R. (2009). Spiking dynamics of bidimensional integrate-and-fire neurons. *SIAM J. on Appl. Dyn. Sys.*, 8(4):1462–1506.

Wan, F. and Tuckwell, H. (1982). Neuronal firing and input variability. *J. Theor. Neurobiol.*, 1(2):197–218.

Wilson, H. (1999). *Spikes, Decisions and Actions: The Dynamical Foundations of Neuroscience*. Oxford University Press, Oxford, U.K.